

CONCENTRATION CONTROL IN MICROFLUIDICS FOR NEUROSCIENCE

APPLICATIONS

By

ALI HASHMI

A thesis submitted in partial fulfillment of  
the requirements for the degree of

MASTER OF SCIENCE IN MECHANICAL ENGINEERING

WASHINGTON STATE UNIVERSITY  
School of Engineering and Computer Science

MAY 2014

To the Faculty of Washington State University:

The members of the Committee appointed to examine the thesis of ALI HASHMI find it satisfactory and recommend that it be accepted.

---

Jie Xu, Ph.D., Chair

---

Rohit Karnik, Ph.D.

---

Stephen Solovitz, Ph.D.

## **ACKNOWLEDGEMENT**

I am highly indebted and grateful to my advisor, Prof. Jie Xu, who has been more of a friend than an advisor to me. Together, we proved a wonderful team; we generated myriads of ideas and some of our best ideas originated as a result of our discussions and scribbling on napkins at dining tables as we continued to explore new places to dine around Vancouver. I have learned many important skills from him, which will continue to benefit me in my future research endeavors. I thank him for realizing and shaping my potential during the course of our interactions.

I thank Prof. Stephen Solovitz for all the mentoring he has provided me with and for his support outside classes. I would take this opportunity to especially thank Prof. Rohit Karnik, who constantly supported me during the course of my thesis.

I thank all the professors here for teaching me numerous courses and with whom I have had a lot of fun interaction while working on other research projects. I would like to extend my gratitude to my colleagues and lab mates, Yuhao Xu and Jiheng Zhao, who taught me the trick and trades of the lab.

Finally, I want to thank my family in Pakistan for their love and support. And, although my working habit limited my Skype conversation with my family on the weekends - one complaint my parents often had with me - I wish to tell them that I cannot repay or thank them enough for everything they have done for me.

# CONCENTRATION CONTROL IN MICROFLUIDICS FOR NEUROSCIENCE

## APPLICATIONS

### ABSTRACT

by Ali Hashmi, M.S.  
Washington State University  
May 2014

Chair: Jie Xu

Achieving a controlled chemical stimulation of neurons is quintessential to understanding how neurons behave to various chemical cues. Unlike traditional technologies, microfluidics allows precise manipulation of fluids at the microscale. In this study, proper actuation mechanisms were sought for a microfluidic platform that can be used for generating spatiotemporally varying chemical concentration gradients. Firstly, piezoelectric actuation is investigated owing to its tendency for enabling faster chemical actuation. Although a relatively faster chemical actuation was attained, issues with the robustness of the piezoelectric transducers were reported. Secondly, a system of two synchronized pumps were utilized to generate a triangular concentration waveform of calcium ions at a constant total flow rate. The generation of a controlled chemical cue is the first step toward the development of a dynamic chemical clamp. The clamp will be used in future to study the effects of various chemical cues (neuromodulators/drugs/ions) on neurons and other cells types. Moreover, the clamp will possibly give insights on the ways neurons interact with cells over long time durations in response to specific chemical cues.

## TABLE OF CONTENTS

	Page
ACKNOWLEDGEMENT .....	iii
ABSTRACT.....	iv
LIST OF FIGURES .....	vii
CHAPTER 1 INTRODUCTION .....	1
1.1 Conventional techniques and challenges in neuroscience .....	2
1.2 Microfluidics and neuroscience .....	3
1.3 Challenges in microfluidics .....	6
1.4 Outline.....	6
CHAPTER 2 SPATIOTEMPORAL CONCENTRATION CONTROL VIA PIEZOELECTRIC ACTUATION .....	8
2.1 Diffusion and Mixing Indices .....	8
2.2 Piezoelectric chemical switch .....	26
CHAPTER 3 SPATIOTEMPORAL CONCENTRATION CONTROL VIA SYNCHRONIZED PUMPS .....	41
3.1 Introduction.....	41
3.2 Advection.....	42
3.3 Setup Validation.....	46
3.4 Device fabrication.....	49

3.5 Experimental results.....	53
CHAPTER 4 CONCLUSION AND FUTURE PERSPECTIVES .....	59
4.1 Summary .....	59
4.2 Future perspectives .....	62
APPENDIX.....	65
BIBLIOGRAPHY .....	85

## LIST OF FIGURES

Figure 1: The image shows the structure of a neuron. (Courtesy: Wikipedia) .....	2
Figure 2: The image shows a microfluidic co-culture chamber wherein different chemical cues can be provided to axons and somal sides of a neurons independently <sup>23</sup> . .....	4
Figure 3: Spatial chemical concentration gradient generators <sup>25,29</sup> .....	5
Figure 4: The sketch shows analyte molecules diffusing across the interface of region A and B. The concentration gradient over the width of the channel attenuates as the fluid moves downstream of the channel; this can be deduced analytically by solving the diffusion equation in 1-D from $x_{min}$ to $x_{max}$ .....	9
Figure 5: Spatiotemporal concentration gradient profiles along the T-channel. (Find Matlab code in Appendix A) .....	11
Figure 6: (left) the sketch shows the T-channel used for simulating diffusion of glutamate in de-ionized water. The depth of the channel is 1 mm. (right) the T-channel was discretized into a mesh using 25844 elements. ....	13
Figure 7: The plot outlines the concentration gradient along the width of the channel as the fluid parcel moves down the long section of the T-channel. The trend suggests that with the passage of time diffusion causes more glutamate molecules to migrate across the interface (marked by a decrease in the gradient of the glutamate mass fraction). ....	15
Figure 8: A PDMS device comprising of a sealed T-channel is prepared via standard soft-lithography. ....	16
Figure 9: Images (a-c) of the flow inside the channel are shot at three different flow-rates (0.5, 0.05 and 0.005 ml/min respectively). The darker region represents the Erioglaurine disodium salt solution whereas the lighter region represents de-ionized water. The sharp interface supports the	

notion that diffusion is minimized at relatively higher flow-rates. (d) shows a histogram of the pixel intensity at the different flow-rates. The frequency of the maximum and the minimum intensities clearly decreases with the flow-rate as more analyte molecules diffuse between the extrema. (Matlab code in Appendix B).....	17
Figure 10: The graph above shows grayscale values plotted versus normalized width of the channel. The variation in the grayscale values over time can be considered as a variation in the concentration of analyte as it diffuse across the channel. The profile qualitatively conforms to that in Figure 5. (Find Matlab Code in Appendix C).....	18
Figure 11: (left) the schematic of a simple T-channel utilized for the experiments. (Right) the sequence of images shows the diffusion of blue dyed solution in water at three different time intervals, with the first image representing the unmixed case. ....	23
Figure 12: The graphs delineate the RMI and AMI for the same mixing event at different light intensities under different types of microscopes. Significant deviation between AMIs and an excellent agreement between the RMIs advocate the use of RMI as a measure of the mixing extent. (MATLAB code in appendix D) .....	24
Figure 13: The image shows the device design for the fast chemical switch. Both the Nozzle and the T-channel are 500 um deep and a depth ratio of 4:1 was chosen to provide substantial displacement of fluid from the chamber to the microfluidic nozzle. ....	27
Figure 14: The image shows the PDMS microfluidic device sealed and clamped with PMMA blocks on the top and the bottom. The top block has holes to allow for microfluidic connects. A piezoelectric transducer is sandwiched between the PMMA block and the double-sided tape. The fluidic chamber is filled with dye and is separated from the T-channel via a microfluidic nozzle. ....	28



Figure 15: Sequence of images above shows shifting of the dye boundary with respect to time for a 1 Hz voltage signal. For the particular experiment, the flow-rate of DI water at the T-channel inlets was maintained at 0.01 ml/min. ....	30
Figure 16: (a) (left) Gray scale intensities versus time for the case when a 1 Hz voltage signal is applied to the piezoelectric bender. (a) (Right) a corresponding spectrogram showing distribution of frequencies in the frequency and time domain. (b) (Left) Gray scale intensities versus time for the case when a 5 Hz voltage signal is supplied. (a) (Right) Corresponding spectrogram depicting frequency distribution in the frequency space and time domain. (Appendix E) .....	31
Figure 17: (a) the sequence of images show a time-wise variation in the colour of the dye stream at a given point of interest (marked in yellow). (b) Similar values of maximum and minimum pixel intensities over a considerable period suggest a stable temporal concentration gradient....	33
Figure 18: an estimate on the number of pixels making up the plume structure is obtained for two consecutive dilation and expansion cycles. (a) An estimated 18605 pixels enveloping the cloud of dye is obtained when the piezoelectric bender underwent relaxation and the dye chamber expanded (b) 21279 pixel count is obtained when the chamber underwent compression. Note: at low actuation frequency $\sim 1$ Hz, an almost constant difference between pixel counts is observed for a considerable duration of device operation.....	35
Figure 19: (a) The graph depicts how the pixel intensity changes when a 1 Hz square voltage signal with 50 % duty cycle is applied to the piezoelectric transducer; expansion phase is sudden – pixel intensities fall abruptly – whereas relaxation period is relatively long owing to the 50 % duty cycle as can be seen by a gradual rise in pixel intensity (b) At higher frequency, 8 Hz with a 50 % duty cycle, the pixel intensities fall with respect to time as more and more ink is pushed farther away from the nozzle and the point of interest.....	37

Figure 20: The chemical pulse is released into the channel. The pulse subsides as the piezoelectric bender causes the chamber to expand. A second pulse follows the first one after a brief time lapse.....	39
Figure 21: A plot showing pixel intensity versus time for the chemical pulses. A reasonable consistency in waveform can be observed for the duration considered.....	40
Figure 22: The graph above represents the requisite flow-rate conditions for two fluid streams to generate a ramp concentration waveform. While the fluid stream with the analyte is ramped up (blue), the DI water stream (green) is ramped down generating a triangular concentration profile at a constant total flow-rate (red). ....	42
Figure 23: The surface profile depicts the normalized concentration profile of Calcium ions across the length and width of the microchannel (1 mm) during the first 0.5 seconds while the flow-rate of the fluid stream with the analyte molecules is ramped up to a maximum 0.6 mL/min. Owing to a small transverse diffusion coefficient and the duration considered, it can be inferred that the calcium ions will not diffuse significantly across the width of the microchannel. ....	44
Figure 24: The surfaces delineate normalized concentration profiles at two different time instances with artificial diffusion coefficients and the markers show the normalized concentration in the middle of the channel at a distance of 2.86 mm from the entrance: (top image) a normalized concentration of 0.3077 at 0.4 sec (bottom) a normalized concentration of 0.3535 at $t = 0.5$ sec. ....	45
Figure 25: The graph represents the change in pixel intensity as the local concentration of Erioglaucine di-sodium salt varies across the width of the microchannel. The intensity variation can be used indirectly to infer information for the analyte. The chemical waveform is	

approximately triangular which is in accordance with the expectation. Higher frequencies in the signal may be due to rapid fluctuations in the light settings .....47

Figure 26: Method of least squares is used to determine the extent to which the chemical waveform conforms to a ramp/triangular shape. The gradients of 37.00 and -38.79 as well as an average  $R^2$  value of 0.744 suggest it is reasonable to assume a triangular waveform .....48

Figure 27: A sinusoidal regression of the same data set (as in Figure 25) results in an  $R^2$  value of 0.702. A sinusoidal fit is more realistic because the pumps cannot have an infinite acceleration. .... 49

Figure 28: (a) Schematic of the device (b) actual device used for sensing  $Ca^{2+}$  ion concentration gradients in a microchannel. The device – comparable in size to a dime - comprises of a 1 mm wide channel and houses electrodes along which SWCNTs are deposited. .... 53

Figure 29: The image shows the experimental setup: two NE 1000X programmable syringe pumps are used to ramp and dispense Calcium ion solution and DI water into the microchannel. A probe station connected to a semiconductor device analyzer is used to collect the current from the CNT sensors and display a resistance time graph. .... 54

Figure 30: The curve shows the resistance change of CNTs during a 90 sec operation. The periodic fluctuation in the resistance change is  $\sim 1$  Hz. A bias can be detected due to which the average of the resistance change steps up in time. The inset shows the moving average in the resistance change. .... 56

Figure 31: The graph shows the single sided frequency distribution of the signal. Amplitude for frequencies lower than 5 Hz, especially 1 Hz is relatively larger compared to higher frequencies, which implies that no extra filtering is needed. (Refer to Appendix H)..... 57

Figure 32: The filtered signal, corrected for the moving average, shows the relative change in resistance of the CNTs. (Appendix I) .....	58
Figure 33: Proposed dynamic clamp feedback loop for neurochemical modulation. A chemical input is supplied to a cell and its response is fed to a mathematical model which affects the input chemical concentration akin to a live neuron. ....	64

## **CHAPTER 1 INTRODUCTION**

Neuroscience or the study of the nervous system holds the key to understanding and curing myriads of diseases, and to unlocking answers to some challenging questions. How does a neuronal connectome store information and coordinate to maintain bodily functions? A better understanding of neuronal connectome also has the potential to addressing the mysteries of consciousness and its origins.

However, to solve such grave questions that involve complex neuronal networks, we would first need to have an accurate understanding of how an isolated neuron behaves in response to an external stimulus. Starting from the basic, more complexity can be further added to get a better image of how a collection of neurons respond in a cooperative manner.

The task of a neuron, merely speaking, is to convey information. In doing so, neurons (Figure 1) utilize both electrical signals and special chemical messengers, known as neurotransmitters.

Electric signals (commonly known as action potentials) travel along a neuron's membrane, down the axon, and eventually cause the neuron to release neurotransmitters at its branched end called dendrites – into a tiny gap called a synapse. Usually through neurotransmitters, one neuron can communicate with and transfer information to adjoining neurons. There are variously many neurotransmitters, such as acetylcholine, dopamine, serotonin, glutamate, endorphins etc...

However, all neurotransmitters can be classified as either excitatory - i.e. they induce action potential in a neuron upon absorption - or inhibitory – i.e. they cease the transfer of information upon absorption.

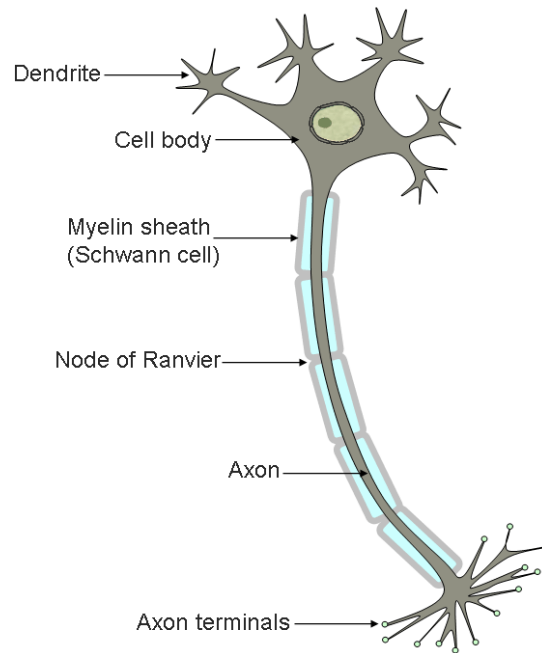


Figure 1: The image shows the structure of a neuron. (Courtesy: Wikipedia)

### 1.1 Conventional techniques and challenges in neuroscience

Traditional research in neuroscience usually involves handling a neuronal culture rather than a single neuron. Brain slices are usually cut to a thickness of a few micrometers. The slice is then cultured in a petri-dish which has all the essential nutrients to keep the cells alive for a few hours. Fluorescent biomarkers and staining methods are employed to identify neurons, and microscopy techniques like optical, confocal and two-photon microscopy are used to identify the firing pattern in the neuronal networks<sup>1</sup>. These techniques have enabled neuroscientists to probe a large ensemble of neurons. With the advent of sophisticated techniques such as optogenetics, much is being discovered about the functions of human connectome. Even though traditional research methods in neuroscience are almost indispensable, they have not been able to resolve

one critical issue: to study the behaviour of a neuron in isolation or even a very small set of neurons. Then there is a secondary, but almost as critical an issue: traditional techniques like patch clamp methods have only enabled researchers to excite neurons electrically<sup>2</sup>. As a corollary to the previous statement, information regarding the response of neurons to certain neurotransmitters, drugs and external agents cannot be obtained if we limit ourselves to conventional methods. Furthermore, the responses of neurons to chemicals - especially neurotransmitters - are on the same order of magnitude as the action potentials i.e. a few milliseconds. Thus, to get precise information researchers would need to use platforms where both chemical stimulation and sampling rate of the measurements are at least 1 kHz.

In developing a platform for neurochemical modulation the first constraint to address is the generation of specific periodic concentration signals – akin to electrical signals. The second constraint is to be able to produce chemical concentration waveforms on the same time-scale as the action potentials.

## **1.2 Microfluidics and neuroscience**

To overcome the aforementioned constraints, we can take advantage of the emergent discipline of microfluidics<sup>3 4</sup> - which deals specifically with the behavior, precise control and manipulation of small volumes of fluids in microchannels. Microfluidics as a tool offers us the ability to shrink huge laboratory spaces and equipment onto a tiny chip<sup>3,5-13</sup>.

In recent years a number of microfluidic platforms have been devised for neuroscience applications: organisms with simple neuronal networks can now be conveniently studied. For instance, optogenetics has been miniaturized to achieve optical control of neurons and muscles in model organisms like *C. elegans*<sup>14</sup>, which can further yield important cues regarding

transmission in synapsis during muscle movement<sup>15,16</sup>. In fact, microfluidic techniques have now made it possible to orient these microscopic organisms laterally to observe critical events e.g. development of neuronal networks and neurodegeneration<sup>17</sup>. With controlled chemical cues in microfluidics, the clustering behaviour of specific neurochemical receptors can now be imaged<sup>18</sup>. Where traditional co-culture setups fail to provide constant perfusion and controlled delivery of oxygen and essential nutrients to the culture in petri dishes, radical biocompatible designs in co-culture chambers ensure constant perfusion without the need for human intervention<sup>19</sup>. Segmented microfluidic platforms can be used to investigate neuronal-glia interactions<sup>20</sup> at an unprecedented level. Furthermore, segmentation in co-culture chambers (Figure 2) has also enabled researchers to study behavioral patterns of axons and cell bodies independently of one another by providing specific chemical cues to regions of interest<sup>21</sup>. It is hoped that microfluidics will continue to offer new avenues in research in neuroscience<sup>22</sup>.

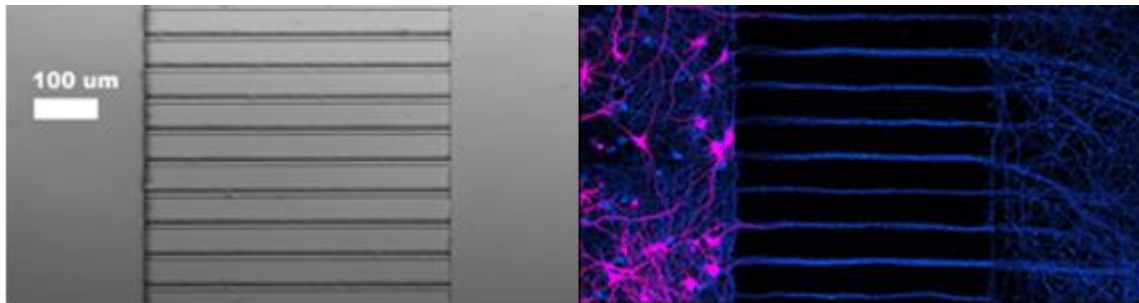


Figure 2: The image shows a microfluidic co-culture chamber wherein different chemical cues can be provided to axons and somal sides of a neurons independently<sup>23</sup>.

In order to identify the effects of chemical agents on neurons, various studies have been conducted in recent years to specifically generate bio-molecular gradients on miniaturized



platforms<sup>19,24-28</sup>. Despite their versatility in providing new insights, a problem unique to all is that nearly all the gradients are steady-state – i.e. they remain constant spatiotemporally (Figure 3). Owing to this reason a number of factors such as temporal variation of chemicals (drugs, neurotransmitters) and the effects on neurons thereof cannot be investigated.



Figure 3: Spatial chemical concentration gradient generators<sup>25,29</sup>

Spatiotemporal variations in chemical cues have yet to be exploited for neuroscience applications. Even platforms that currently have the capability for producing spatiotemporally varying concentration gradients are indeed complex devices. A simple mechanism does exist; Botzolakakis et al devised a microfluidic platform comprising of a stepper motor to generate concentration waveforms with an actuation frequency of  $\sim 20$  Hz<sup>30</sup>. However, it is highly unlikely to generate complex waveforms reliably using a single stepper motor driven pump. Thus, it is important to develop platforms wherein chemical gradients can be conveniently generated and tweaked spatiotemporally, preferably at higher actuation frequencies in real-time.

### **1.3 Challenges in microfluidics**

However, getting small has its own problems. In most applications, we need to acquire certain reagents, transport and manipulate them using our hands or robots. At small scale it is extremely challenging to effectively access, sort, manipulate and especially mix ingredients. There are primarily two issues that need to be addressed before we can realize a platform for generating rapid spatiotemporally varying concentration gradients. Firstly, to determine an appropriate mechanism that can reduce the actuation time-scale to the same order of magnitude as the action potential. Secondly, since inertial effects are negligibly small for flows at low Reynolds number<sup>3</sup>, it is necessary to ensure and enhance mixing of chemicals (analytes) as the fluid flow through the microchannels.

### **1.4 Outline**

In this thesis, two different actuation methods, namely piezoelectric actuation and synchronized mechanical pumps, were employed to generate spatiotemporal variations in chemical concentrations. Subsequent sections discuss and characterize the two methodologies in detail. As an outline, Chapter 2 begins by exploring the notion of diffusion in microchannels. The concept of mixing indices will be introduced to the reader to quantify the extent of mixing. Different devices based on piezoelectric transducers will be utilized to generate a spatiotemporal concentration gradient and their performance will be evaluated. Chapter 3 introduces a different actuation scheme wherein two synchronized mechanical pumps will be used to generate a triangular concentration waveform of  $\text{Ca}^{2+}$  ions. The setup was first validated with the use of a coloured dye. A nanosensor was used later to assess the performance of the pumps in generating

the required chemical signal. Chapter 4 presents a brief comparison of the two methods, and it offers suggestions for improvement and a framework for a novel dynamic clamp method.

## CHAPTER 2 SPATIOTEMPORAL CONCENTRATION CONTROL VIA PIEZOELECTRIC ACTUATION

### 2.1 Diffusion and Mixing Indices

Diffusion of analyte across a fluid-fluid interface can be understood by considering the solution to the diffusion equation (1), which theoretically predicts the population of molecules that can permeate across an interface while a concentration gradient exists.

$$\frac{\partial C}{\partial t} = D \left( \frac{\partial^2 C}{\partial x^2} \right) \quad (1)$$

where,  $C$  represents the analyte concentration,  $x$  and  $t$  represent the space and time coordinates respectively, and  $D$  represents the diffusion constant (specific to the analyte and liquid media).

For the case wherein analyte molecules are diffusing across an interface during flow in a channel, the spatiotemporal concentration distribution of the analyte can be obtained analytically by solving (1). For simplicity two bulk liquid media (one with and the other without analyte) flowing in a T-channel are represented as sketched (Figure 4) with appropriate initial conditions and boundary conditions listed.

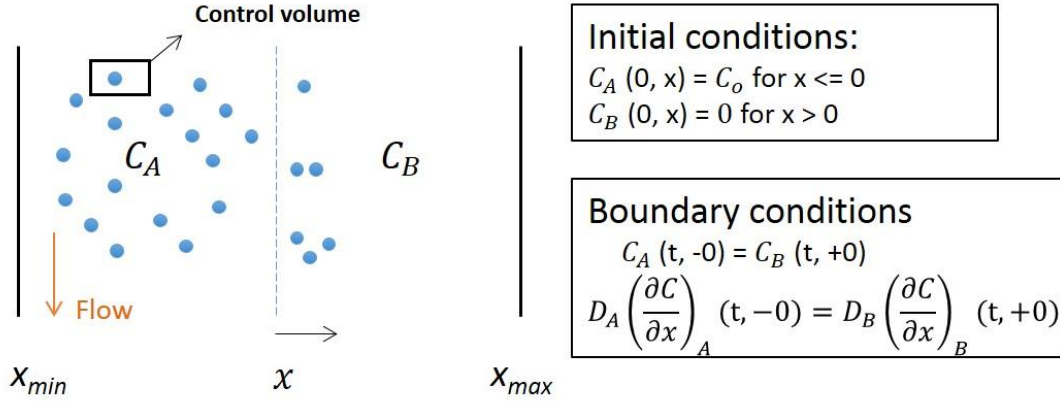


Figure 4: The sketch shows analyte molecules diffusing across the interface of region A and B. The concentration gradient over the width of the channel attenuates as the fluid moves downstream of the channel; this can be deduced analytically by solving the diffusion equation in 1-D from  $x_{min}$  to  $x_{max}$

Since the distance of the boundaries from the center of the channel are much larger in magnitude compared to the length-scale of the analyte molecule, the diffusion equation can be solved using the method of self-similar solutions. The initial conditions and boundary conditions are substituted to yield the following expressions for the dimensionless analyte concentration:

$$\frac{C_A}{C_o} = 1 - \frac{1}{2} \left( 1 + \text{Erf} \left( \frac{x}{2\sqrt{D_A t}} \right) \right) \quad (2)$$

$$\frac{C_B}{C_o} = \frac{1}{2} \text{Erfc} \left( \frac{x}{2\sqrt{D_B t}} \right) \quad (3)$$

For the case when the liquid media in both A and B are the same, the problem is further simplified as  $D_A = D_B = D$ .

To be able to extract a solution, two parameters need to be known: the diffusion coefficient and the period for which the flow is considered. The former can be calculated using the Stokes-Einstein equation, whereas the latter is the time ( $t$ ) taken by a fluid parcel to enter and escape the T-channel and is estimated by:

$$t = \frac{L \cdot A}{Q} \quad (4)$$

Where,  $L$  and  $A$  are the length and the cross-sectional area of the T-channel, and  $Q$  is the volume flow-rate inside the T-channel.

The flow-rate in the channel can be adjusted to alter the fluid velocity and hence control the spatial distribution of the analyte along the length of the T-channel. In addition, in order to predict a specific spatial concentration profile along the length of the channel, only the type of analyte (e.g. a neurotransmitter, drug molecule or a nutrient) and the channel geometry needs to be specified.

For instance, the diffusion coefficient for glutamate molecules (an important neurotransmitter associated with memory and learning) in aqueous medium is generally assumed to be  $7.5 \times 10^{-10} \text{ m}^2/\text{s}$ <sup>31</sup>. Computation involving an arbitrary time period using (2) and (3) can yield information regarding how normalized glutamate concentration varies spatiotemporally across a liquid-liquid interface along the flow direction. Figure 5 shows a normalized concentration profile of glutamate (GABA) across a 4 mm wide channel.

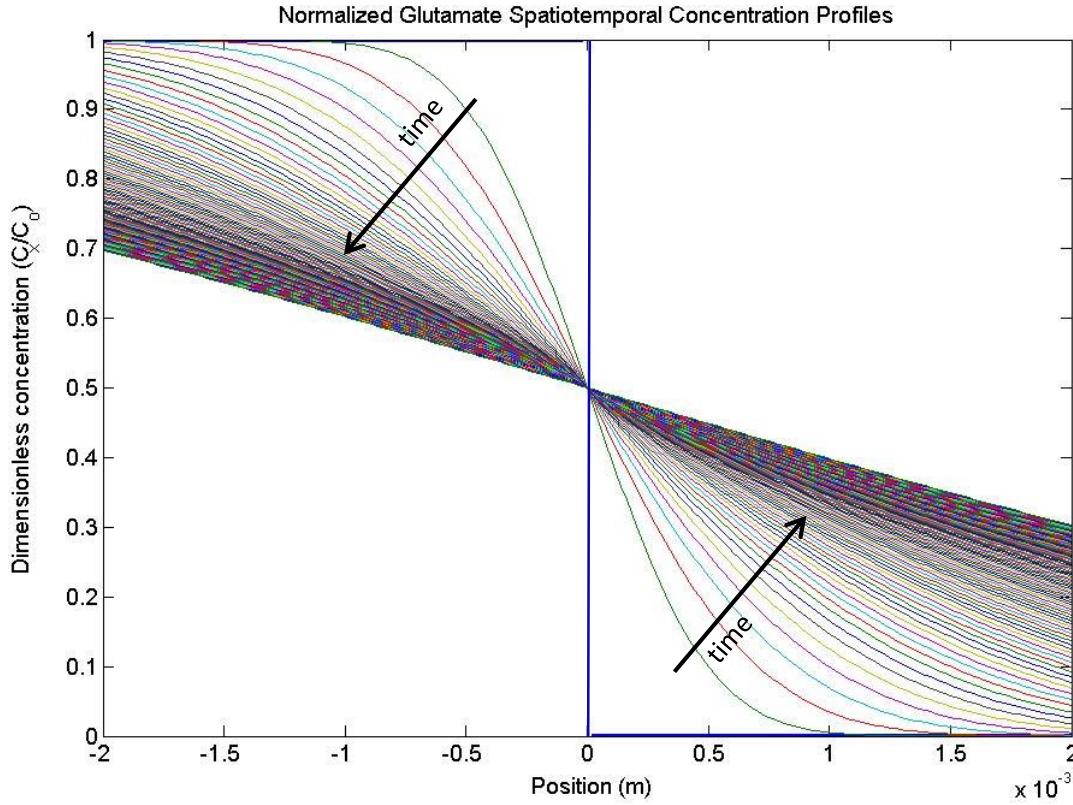


Figure 5: Spatiotemporal concentration gradient profiles along the T-channel. (Find Matlab code in Appendix A)

The graph shows the normalized spatiotemporal concentration profile as the glutamate molecules diffuse from a concentrated aqueous glutamate solution to a DI water stream. Note that for a given point in space the concentration profile is steady state; the various curves represent the normalized concentration profiles over the width of the T-channel as the control volume sweeps downstream with fluid flow. For an infinitely long channel the concentration gradient would eventually tend to zero. However, because in reality the T-channel can only be a few mm long, thus only the first few spatiotemporal profiles are the representatives of the actual concentration gradients.

Concentration gradients within the T-channel can be easily manipulated by varying the flow speed or the Reynolds number (Re). By increasing the flow-rate, the Peclet number (Pe) – defined as the ratio of convection to diffusion (5) - increases. As a consequence, not many molecules will be able to diffuse across the interface and hence, the concentration gradient will remain considerably large throughout the length of the T-channel. On the contrary, a reduced flow-rate in the T-channel decreases the Pe number and thus, allows the concentration gradient to flatten out more along the length of the channel.

$$Pe = \frac{W \cdot U}{D} \quad (5)$$

where  $W$  is the channel-width,  $U$  is the average fluid velocity and  $D$  is the diffusion constant

A measure of the spatiotemporal chemical concentration can be obtained via simulation. Simulation for the mixing of GABA solution and water in a T-channel is performed using ANSYS FLUENT 14.0. A T-channel is created in SolidWorks as shown in Figure 6 (left). Meshing of the geometry was done using 25,844 cubic elements with 831,096 nodes (Figure 6, right). Species transport model along with viscous laminar flow was utilized to simulate the mixing of a water stream with a 0.1 % mass glutamate solution. Created as a pseudo-fluid, three properties – density, molecular weight, and viscosity - were defined for glutamate. A mixture template was used to combine liquid water and the glutamate fluid together to produce the mixture. The viscosity of glutamate fluid was set equal to that of water since an aqueous 0.1 % mass glutamate solution is assumed dilute. The viscosity of the mixture-template was set as a constant with magnitude equal to that of water at room temperature and pressure and the mass diffusivity was set to  $7.5 \times 10^{-10} \text{ m}^2/\text{s}$ . Volume-weighted mixing law was enabled before the



boundary conditions were defined.

A simulation was performed, with a 0.1 % mass GABA solution entering from one inlet port and DI water entering from the second, for a Re number of 0.0716 and corresponding Pe number of 96.

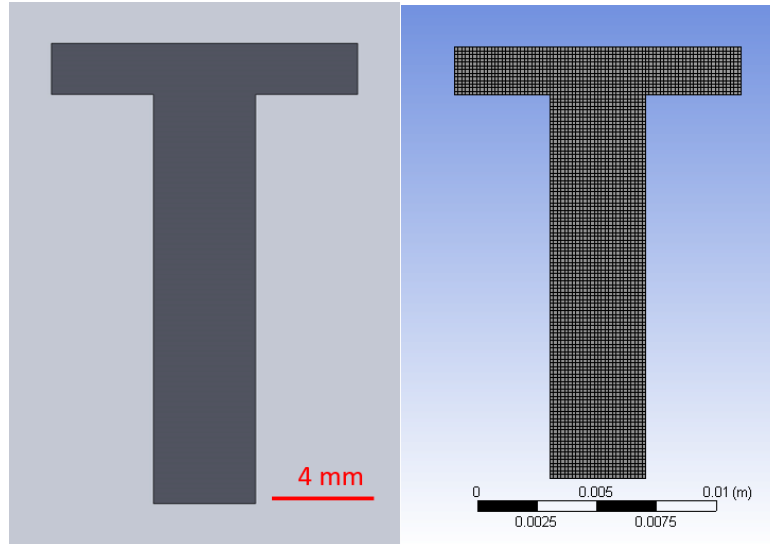


Figure 6: (left) the sketch shows the T-channel used for simulating diffusion of glutamate in de-ionized water. The depth of the channel is 1 mm. (right) the T-channel was discretized into a mesh using 25844 elements.

The graph in Figure 7 depicts the simulation result. The x-axis shows the position across the long section of the T-channel and the y-axis represents the glutamate mass fraction. The dashed lines delineate the variation in the glutamate mass fraction from the inlet ports to the outlet port of the T-mixer. An image in the inset of the figure shows a visual representation of glutamate diffusing across the channel during the flow. The red colour indicates a glutamate mass fraction of 0.1

whereas the blue colour depicts a glutamate mass fraction of 0 and likewise, the green zone represents the intermediate mass fraction of glutamate.

As can be inferred from Figure 7, more and more glutamate diffuses across the interface along the channel. The concentration gradient decreases downstream of the flow owing to the migration of glutamate molecules. The trend here is similar to that determined in Figure 5, with the difference that a glutamate mass fraction is plotted against the width of the channel rather than a normalized concentration profile.

It is not difficult to demonstrate that as the fluid parcels take more time to flow through the T-channel - at low  $Re$  - diffusion will allow glutamate molecules to mix more. On the other hand, convection dominates at higher  $Re$  values and the glutamate molecules lack sufficient time to diffuse across the liquid-liquid interface.

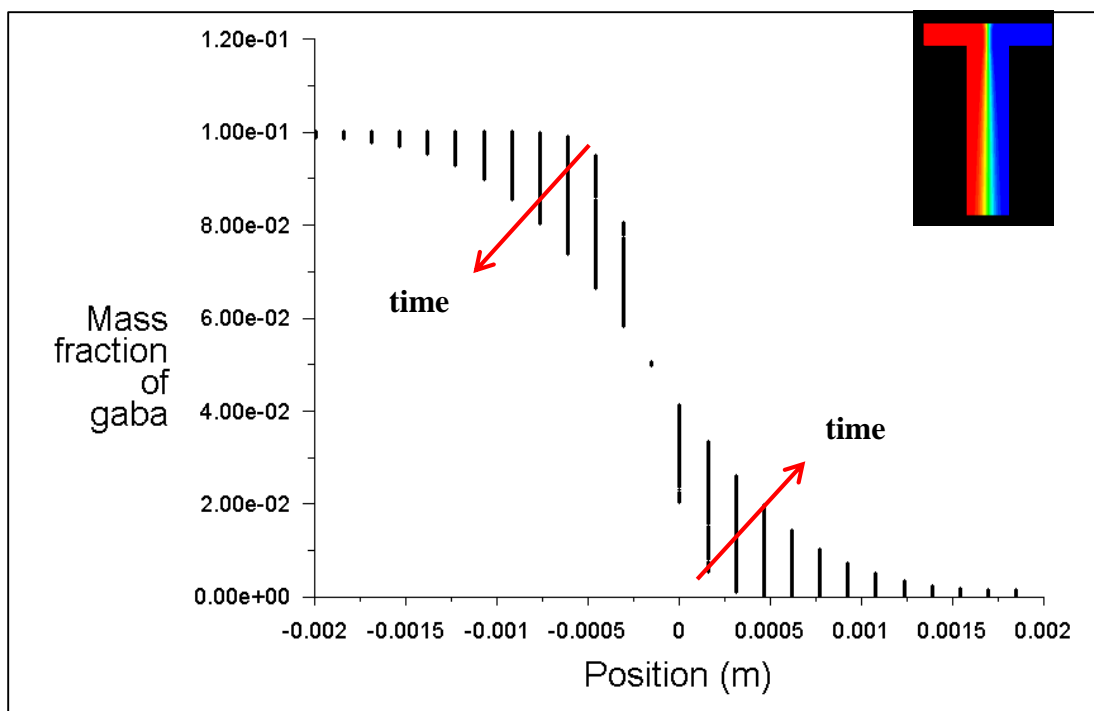


Figure 7: The plot outlines the concentration gradient along the width of the channel as the fluid parcel moves down the long section of the T-channel. The trend suggests that with the passage of time diffusion causes more glutamate molecules to migrate across the interface (marked by a decrease in the gradient of the glutamate mass fraction).

Experiments were performed to visually observe diffusion of analyte from a solution to a DI water stream. For this purpose, a solution was prepared by dissolving 0.157 grams of Erioglaurine disodium salt (blue in colour) in 250 ml of DI water. A T-channel (with the dimensions provided in Figure 6) was fabricated from PDMS (poly di-methyl siloxane) using standard soft-lithography. The PDMS chip with its channel-side plasma bonded to a glass slide and inserts on the top for injecting liquids is shown in Figure 8 below.

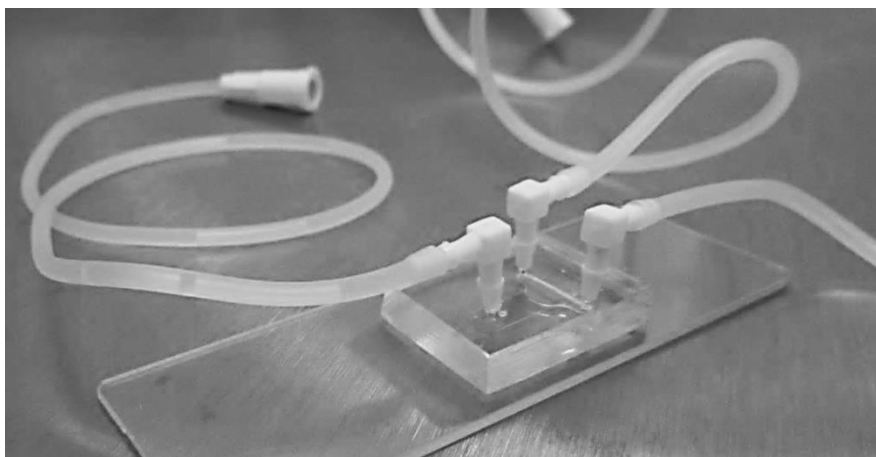


Figure 8: A PDMS device comprising of a sealed T-channel is prepared via standard soft-lithography.

A syringe pump (KDS 210) with programmable flow-rate was used to pump DI-water and Erioglaucine solution into the T-channel and a microscope (Nikon MM400) was used to take coloured images of the liquid-liquid interface inside the channel during the flow.

In the first set of experiments, three different flow rates (0.5 ml/min, to 0.05 ml/min and 0.005 ml/min) were selected to observe the effects of varying flow rate on the diffusive patterns in the channel; Figure 9 (a-c) respectively show the corresponding images in grayscale. Matlab was used to plot the histograms (as shown in Figure 9 (d)) of the pixel intensity (count) versus pixel values for the three images. Note that the same region was selected for obtaining the histograms. As can be seen from the plot, the frequency of both the maximum and minimum pixel intensities decreases with the flow-rate, as more and more analyte molecules diffuse across the extrema.

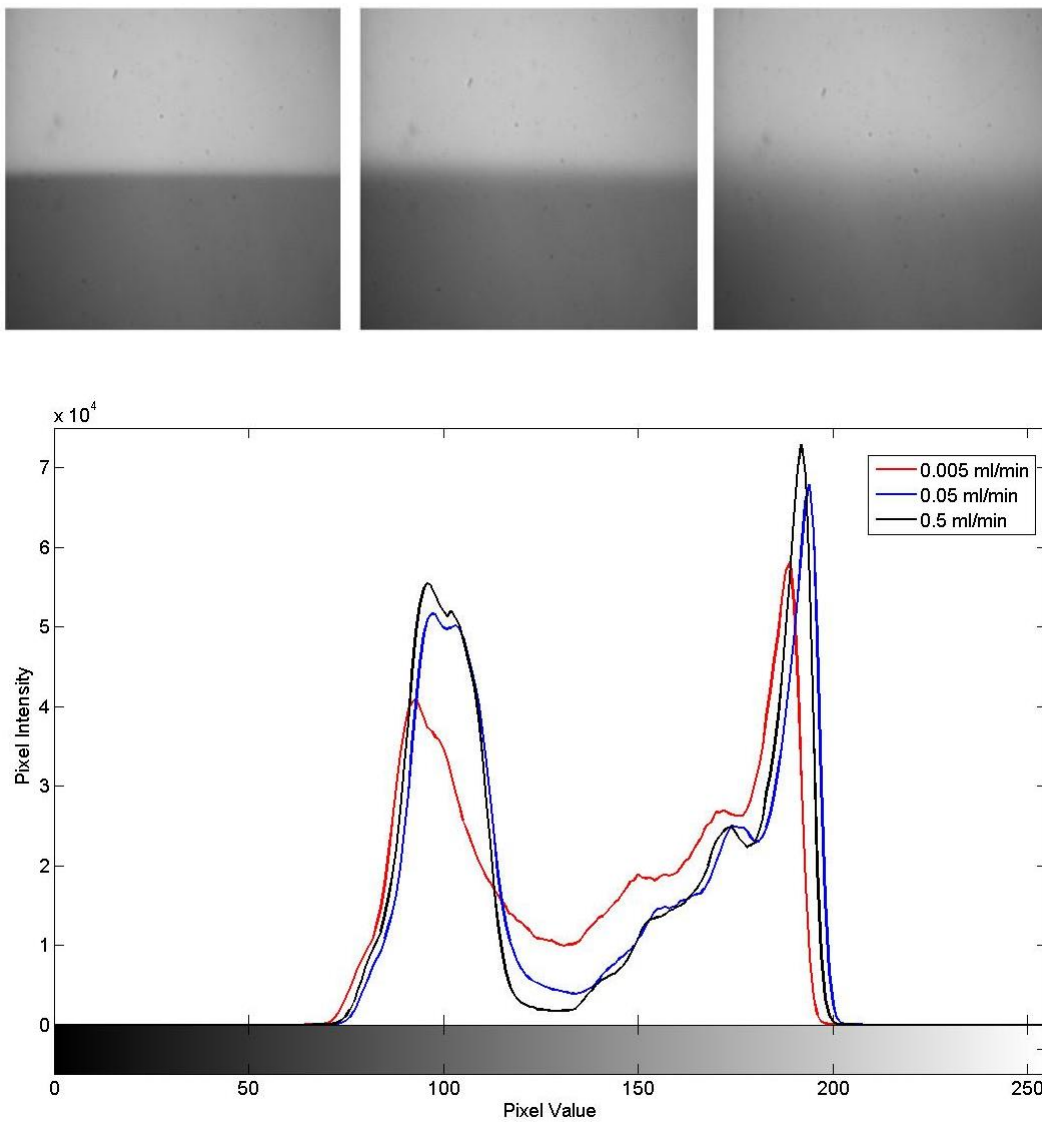


Figure 9: Images (a-c) of the flow inside the channel are shot at three different flow-rates (0.5, 0.05 and 0.005 ml/min respectively). The darker region represents the Erioglaurine disodium salt solution whereas the lighter region represents de-ionized water. The sharp interface supports the notion that diffusion is minimized at relatively higher flow-rates. (d) shows a histogram of the pixel intensity at the different flow-rates. The frequency of the maximum and the minimum intensities clearly decreases with the flow-rate as more analyte molecules diffuse between the

extrema. (Matlab code in Appendix B)

Similarly, an entire diffusion event can be mapped by stopping the flow in the channel and taking time-lapse images of the evolution of the dye profile. In a second set of experiment the flow (originally 0.5 ml/min) was stopped and the dye profile was recorded after every 30 seconds for 6.5 minutes. The last two images are taken 2 minutes apart. Subsequently, the diffusion profiles due to random-walk can be obtained by plotting the mean grayscale values along a defined region that extends across the width of the channel. Figure 10 presents the mean of the grayscale values for the time-elapsd images plotted versus the normalized width of the channel. The graph illustrates that the concentration gradient of analyte decreases with the passage of time in accordance with continuity principle.

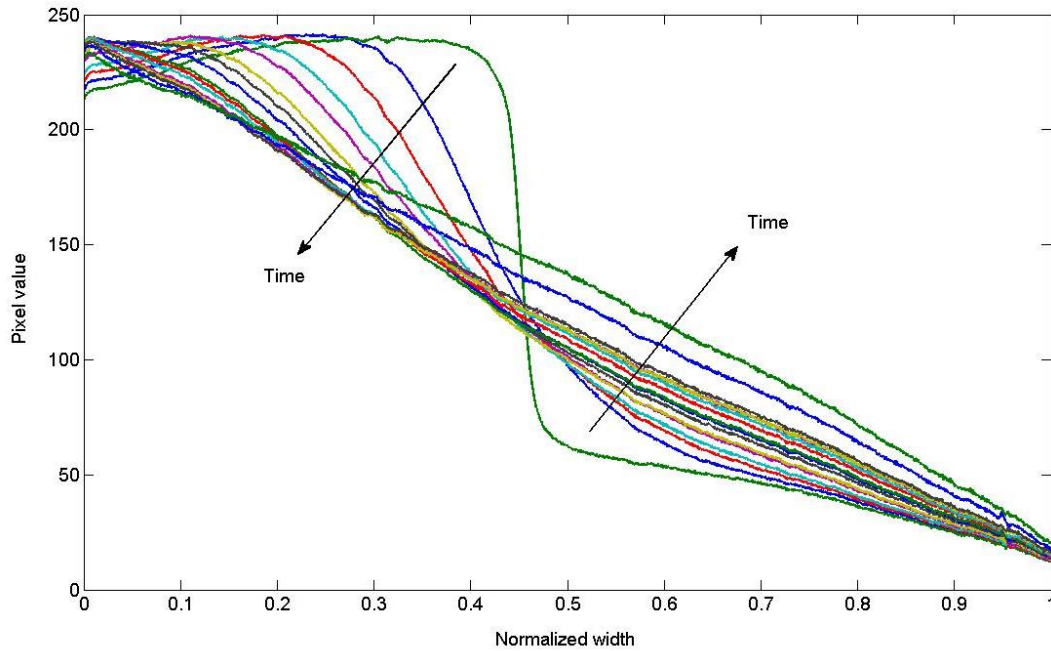


Figure 10: The graph above shows grayscale values plotted versus normalized width of the channel. The variation in the grayscale values over time can be considered as a variation in the

concentration of analyte as it diffuse across the channel. The profile qualitatively conforms to that in Figure 5. (Find Matlab Code in Appendix C)

Mixing is one of the most fundamental challenges in microfluidics due to the laminar flow behaviour at microscale. Enhancing mixing in microfluidics has thus been extensively studied in past two decades, and being a quintessential function will continue to be of interest to the lab on a chip community. Generally speaking, mixing of fluids in microchannels can be achieved using either active or passive mixers<sup>32,33</sup>. Regardless of the mixing mechanism, usually mixing is quantified by processing a set of images to yield a meaningful index that is representative of the extent of mixing. On the images, different fluids are usually differentiated based on differences in light intensities received by a camera. A dye is often used to absorb transmitted light, reflect incoming light or emit light itself for the camera recording. However, the extent of mixing remains incomparable throughout the wide spectrum of studies on microfluidic mixing. Indeed, none of the review papers have directly compared the mixing effects from different studies and a few are replete with misleading comparisons. Why we cannot compare mixing events across different studies, even if the researchers use the same mixing quantification method, is primarily due to the following reasons: 1) some mixing quantification methods are very sensitive to the initial mixing conditions - slight interfacial diffusion will influence the value dramatically; 2) some methods give values that depend on the minimum pixel intensity in the image – any mixing event that involves dyes other than black will be problematic; 3) in cases where mixing is not 1:1, some methods will produce values that are out of normal range.

Therefore, there is a need to set a common scale for quantifying the extent of mixing, making comparisons convenient across different studies. Here, we first summarize the various mixing indices and then establish a common index to gauge spatiotemporal mixing events more reliably.

Mixing indices are computed using intensities of pixels across a cross-section of a grayscale image that delineates a mixing event. The simplest index is calculated by taking the standard deviation,  $\sigma$ , of the pixel intensities<sup>34-36</sup>, as shown in equation (6) below:

$$\sigma = \sqrt{\frac{1}{N} \sum_{i=1}^N (I_i - \langle I \rangle)^2} \quad (6)$$

where  $I_i$  shows a local pixel intensity,  $\langle I \rangle$  shows the average of the pixel intensities in the cross-section, and  $N$  represents the total number of pixels.

This index attains the highest value when the fluids are unmixed and 0 if the fluids are homogeneously (completely) mixed. Although a measure of simple standard deviation yields information regarding the spread of data about the mean intensity, it is not a direct measure of the extent of mixing since the index possesses a dimension of intensity and can also be biased by a few large deviations. Hence, comparison of mixing extent among different studies is not possible with the usage of this index.

The index can be rendered dimensionless by comparing the standard deviation to the mean intensity<sup>37-46</sup>. For the sake of discussion, we call the ratio as the “absolute mixing index (AMI)” and it can be computed from the following formula:



$$AMI = \frac{\sigma}{\langle I \rangle} = \frac{\sqrt{\frac{1}{N} \sum_{i=1}^N (I_i - \langle I \rangle)^2}}{\langle I \rangle} \quad (7)$$

The aforementioned mixing index, on a scale of 0-1 (for 1:1 mixing), quantifies mixing where 1 delineates an unmixed state and 0 as a fully mixed state for the case in which one of the fluid streams yields a minimum pixel intensity of 0 (for instance, black ink that absorbs all the incoming light, or a black field without emission of fluorescent light). Note that, some researchers replace  $\langle I \rangle$  with  $I_{\text{mixed}}$  in the equation, which serves the same purpose, since  $I_{\text{mixed}}$  should ideally equal to  $\langle I \rangle$ .

Although AMI is a direct measure of the mixing extent, it still cannot be used for comparing mixing in different studies. For example, two hydrodynamically identical mixing events would result in different absolute mixing indices if different lighting conditions are used, let alone the cases where inks with dissimilar colours are used. Methods that tend to solve this problem include artificially rescaling (stretching) or normalizing each pixel to the same span of intensities as 0-255 on a grayscale image, or 0-1. The mixing index obtained using equations (7) with modified intensity values should be called “absolute mixing index with modified intensities”.

The process of rescaling and stretching intensities makes analysis and comparison an extremely tedious process. Therefore, a third kind of mixing index, which we name here as “relative mixing index (RMI)”<sup>47-50</sup>, precludes the need for any artificial pre-treatment of the intensity data, such as stretching or rescaling. RMI can be computed by taking the ratio of standard deviation of pixel

intensities across a cross section to the standard deviation of the pixel intensities in the unmixed case,  $\sigma_o$ , according to equation (8) as follows:

$$RMI = 1 - \frac{\sigma}{\sigma_o} = 1 - \frac{\sqrt{\frac{1}{N} \sum_{i=1}^N (I_i - \langle I \rangle)^2}}{\sqrt{\frac{1}{N} \sum_{i=1}^N (I_{oi} - \langle I \rangle)^2}} \quad (8)$$

where  $I_{oi}$  represents the local pixel intensity in the unmixed state.

Note that, although the ratio itself is quite versatile in making comparisons of the extent of mixing, it is a rather non-intuitive representation. Thus, a more subtle way to quantify a mixing event is by considering (1– the ratio) in percentage form, which we can characterize as mixing efficiency or mixing ratio, so that the scale of RMI extends from 0 to 1, where 0 delineates the unmixed state and 1 as the homogeneously mixed state.

Experiments were conducted to record a specific mixing event at varied light intensities, with images recorded using two different types of optical microscopes with different lighting direction. The extent of mixing was then compared using both AMI and RMI. A  $7.92 \times 10^{-4}$  Mol/L solution of blue dye (Erioglaucine disodium salt, Acros Organics) was allowed to mix with de ionized (D.I) water in a micro T-channel (Figure 11, left), which was fabricated using PDMS (Polydimethylsiloxane) soft-lithography.

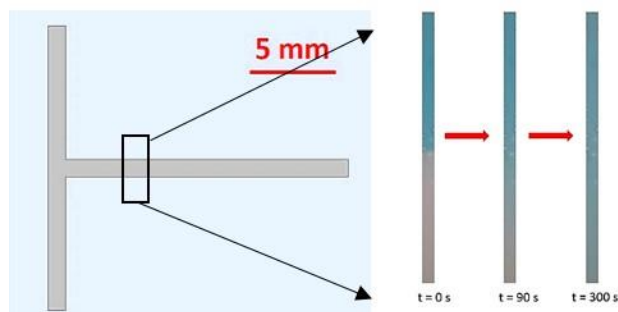


Figure 11: (left) the schematic of a simple T-channel utilized for the experiments. (Right) the sequence of images shows the diffusion of blue dyed solution in water at three different time intervals, with the first image representing the unmixed case.

Holes were punched into the polymer to create inlets and outlets for the passage of fluid. The chip was then plasma-bonded onto a glass slide. Inserts and tubing were attached to the two inlets of the microchannel on one end and to plastic syringes on the other to ensure fluid flow without any leakages. An insert with tubing was attached to the outlet of the T-channel as a means to exhaust fluid. The syringes – one comprising of the blue dyed solution and the second with DI water - were mounted onto a syringe pump (KDS 210). The fluidic chip was placed under a Nikon microscope (MM400) attached to a camera (Nikon DS –Fi2 5 megapixel) to capture videos and images (10 X) in real time. The KDS pump was programmed to dispense fluids at 0.5 mL/min until a sharp interface was observed between the dyed solution and the DI water stream. Significant time was allowed for the system to reach equilibrium before the measurements were made. The image at time  $t=0$  s was taken during the duration the pump was active. The pump was stopped and a stop watch was started; images were taken at various time intervals to capture the entire diffusion event (Figure 11, right). The experiments were performed for varied light intensities (labelled as bright, dark and darkest) using reflected light. Later, an

experiment was performed under a stereomicroscope (Leica EZ4 HD) and images were captured at specified time intervals with transmitted light.

The images were analysed using a Matlab code to determine AMI and RMI. Results for the different cases are presented in Figure 12. As is evident, the AMIs deviate considerably for the same hydrodynamic mixing event at varied light conditions, whereas the computed RMI have an excellent agreement irrespective of the light intensity.

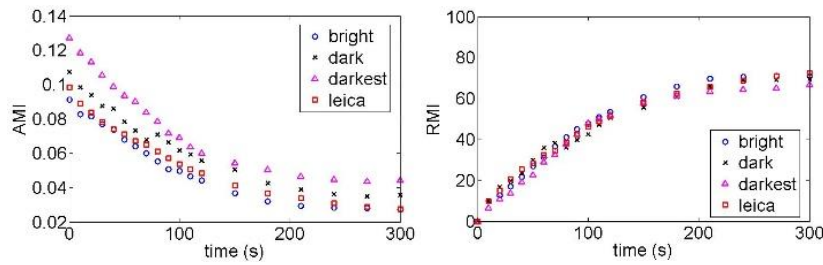


Figure 12: The graphs delineate the RMI and AMI for the same mixing event at different light intensities under different types of microscopes. Significant deviation between AMIs and an excellent agreement between the RMIs advocate the use of RMI as a measure of the mixing extent. (MATLAB code in appendix D)

The caveat regarding the various mixing indices is that the entire characterization of mixing is based on the distribution pattern of the intensity values of the pixels within the span of the minimum and maximum intensities. On the one hand, standard deviation alone can be very different for similar patterns of intensity distribution. On the other hand,  $\langle I \rangle$  is dependent on the light intensities and not necessarily in a linear fashion.

Thus, usage of AMI is not an effective method of quantifying mixing events, except for cases when one of the fluids is absolutely black on the image. However, in RMI the temporally evolving distribution pattern of the pixel intensity values is always compared to the initial distribution. Hence, RMI as index is insensitive to variation in light intensities as well as the colour of the dyes involved, provided the diffusion coefficient remains constant.

Since each biochemical event has its own characteristic time, therefore it is very important to have a clear comparison of mixing extent at different time scales. By quantifying one such mixing event under various light intensities and two different types of optical microscopes, we have demonstrated that AMI is not an accurate representative of the mixing extent. Owing to the insensitivity of RMI to light intensities, dye colour, span of intensity distributions, we will use it in making comparisons for mixing events. Table 1 shows the mixing extent (quantified in terms of RMI) achieved for the first set of experiments (Figure 9).

Table 1: mixing indices computed for the grayscale images in Figure 9.

<b>Flow-rate (ml/min)</b>	<b>Relative Mixing Index</b>
0.5	0 (assumed as unmixed)
0.05	1.5608
0.005	8.4023

From a background study we have determined that diffusion of chemical species is extremely slow at small scale. For faster chemical actuation, diffusion solely cannot ensure sufficient

mixing between chemical species. On the other hand, for relatively slower chemical actuation when concentration gradients need to be maintained for longer periods, diffusion disrupts the desired concentration. Hence, we cannot rely on diffusion alone for generating spatiotemporally varying concentration gradients. Active methods need to be utilized for developing such platforms.

## **2.2 Piezoelectric chemical switch**

A chemical switch was developed using a piezoelectric bender; the purpose of the chemical switch was to dispense chemical packets to create concentration gradients in a channel for a system of two miscible liquids. The motivation was to utilize the faster actuation of piezoelectric benders to stimulate neurons with tunable chemical signals with an unprecedented timescale. The frequency as well as the amplitude of the piezoelectric bender was tuned to generate specific chemical waveforms.

The first concept of the device is presented in the SolidWorks drawing in Figure 13 below.

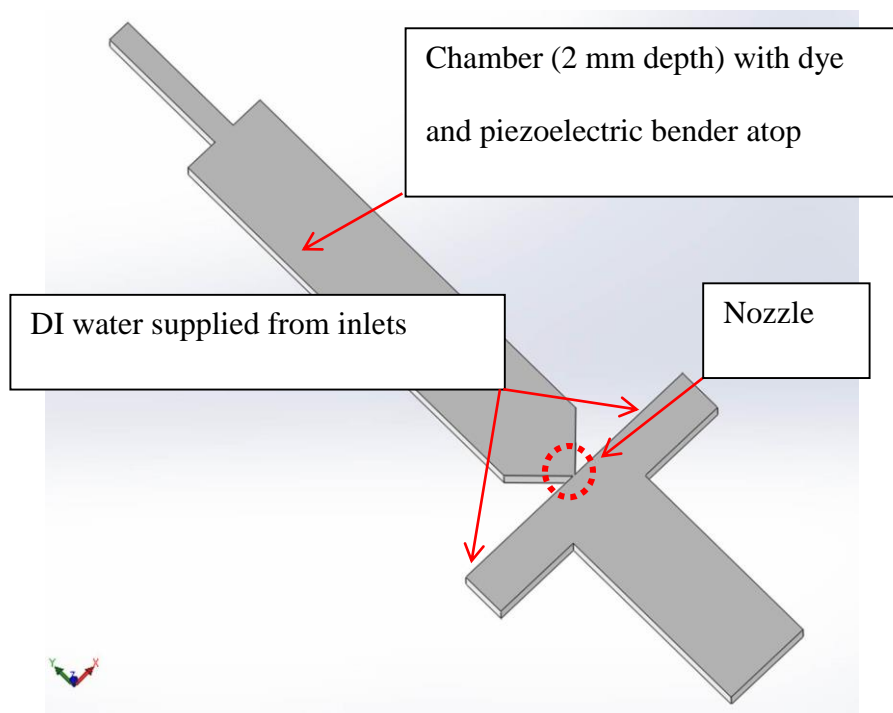


Figure 13: The image shows the device design for the fast chemical switch. Both the Nozzle and the T-channel are 500  $\mu\text{m}$  deep and a depth ratio of 4:1 was chosen to provide substantial displacement of fluid from the chamber to the microfluidic nozzle.

The mold for the device was fabricated using a PMMA chip using conventional micromilling technology with a 3.175 mm milling bit. The actual device was prepared using soft lithography (Figure 14). A thin layer of cellophane was flexed on top of the channel to seal the device. A 500  $\mu\text{m}$  thick piece of piezoelectric transducer was cut accordingly to cover the span of the chemical chamber before the nozzle and attached atop the cellophane sheet using a piece of double-sided tape.

The PDMS device with its sealing was clamped at the base of the channel with a flat piece of

PMMA. A cavity was milled into the PMMA chip to provide some clearance to house the extended length of the piezoelectric transducer. Furthermore, another PMMA block was supplemented on top of the device to prevent bending within PDMS owing to the clamping force. Note the top PMMA block has holes drilled into it to allow for microfluidic connects (in/outlets).

According to theory, the oscillation of the piezoelectric bender would cause the flexible cellophane sheet to bend periodically causing the chamber to contract and expand. The fluid would be expelled via a microfluidic nozzle - which serves to amplify the displacement. The periodic dispensing would generate a spatiotemporally varying chemical gradient.

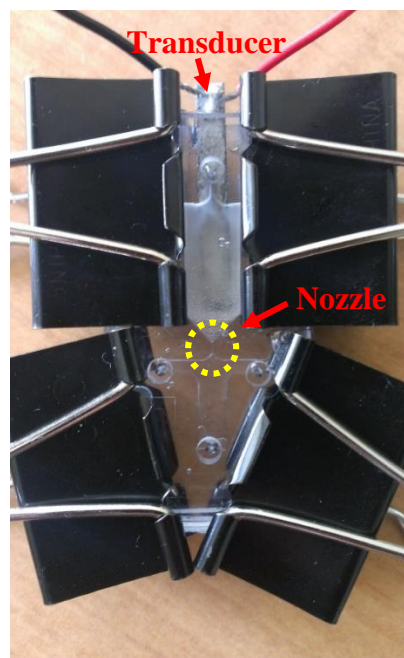


Figure 14: The image shows the PDMS microfluidic device sealed and clamped with PMMA blocks on the top and the bottom. The top block has holes to allow for microfluidic connects. A piezoelectric transducer is sandwiched between the PMMA block and the double-sided tape. The fluidic chamber is filled with dye and is separated from the T-channel via a microfluidic nozzle.



The chamber was filled with Erioglaucine disodium salt solution and DI water was allowed to flow through the inlets of the T-channel. An amplified ramp voltage signal was supplied from the signal generator to the piezoelectric bender. Videos were recorded with a camera (Nikon DS – Fi2 5 megapixel) mounted on Nikon Microscope (MM400). During the experiments, two parameters were varied: the flow-rate of the DI-water (0.01 to 0.05 ml/min) and the frequency of oscillations of the piezoelectric bender (1-50 Hz).

Contrary to expectation, no individual parcels of dye were dispensed from the nozzle. Instead, a constant stream of chemical was observed issuing forth from the nozzle with a periodically shifting boundary. Failure to observe individual dye packets may be attributed to the nozzle shape and/or geometry which perhaps do not ensure appropriate fluid dynamics to cause the jet to break into parcels. Nevertheless, the oscillating chemical boundary can be utilized to locally stimulate cell bodies. The frequencies of such cues are tuneable.

A time evolution of the jet profile for a 1 Hz voltage signal is shown in Figure 15. Owing to the faint blue colour of the dye, the colours in the original images were first split into three channels (Red (R), Green (G) and Blue (B)) and then an edge detection function was applied from the lookup table in Image-J to R channel to make the edges visible. The shifting of the dye boundary (varying distance between the plume and the dashed reference line) is apparent from the images.

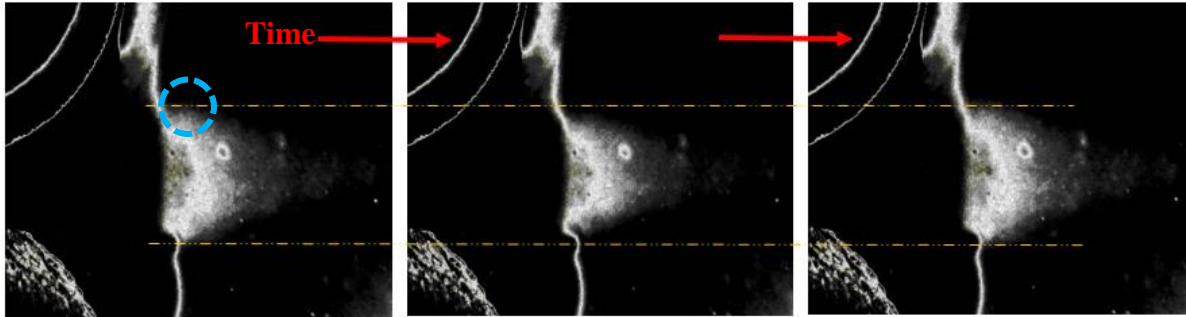


Figure 15: Sequence of images above shows shifting of the dye boundary with respect to time for a 1 Hz voltage signal. For the particular experiment, the flow-rate of DI water at the T-channel inlets was maintained at 0.01 ml/min.

A MATLAB code (see Appendix E) was developed to analyze the sequence of frames in the original recording - first to extract the grayscale intensities (an indirect measure of the chemical concentration) from the images, and second to employ Gabor Transformation (a windowed Fast Fourier Transform) to obtain the spectral distribution in the frequency space and time domain. A location near the plume was considered such that the boundary shift about it was noticeable. The image on the left in Figure 16 (a) shows pixel intensity plotted against time when a 1 Hz ramp voltage signal was applied. As can be delineated from the figure, the occurrence of peaks has a one-to-one correspondence in time.

The average maximum and minimum pixel intensities are approximately 163 and 157 respectively. Notice that the curves are jagged; this may be due to fluctuations in the lighting conditions, camera's shutter speed or scattering of light from particles in the solution. A complementary spectrogram (Figure 16 (a), right) also shows the spread of frequencies in the chemical waveform over 5 seconds of operation. Likewise, at higher frequencies, for instance 5 Hz, approximately 5 cycles are observed per unit time (refer to Figure 16 (b), left). The spectrogram on the right in Figure 16 (b) shows distribution of frequencies in the chemical waveform in both the frequency space and time domain for a case when a 5 Hz voltage signal is applied to the piezoelectric transducer; the low frequencies including 5 Hz are dominant in the spectrum as evident by the bright instances centered about zero.

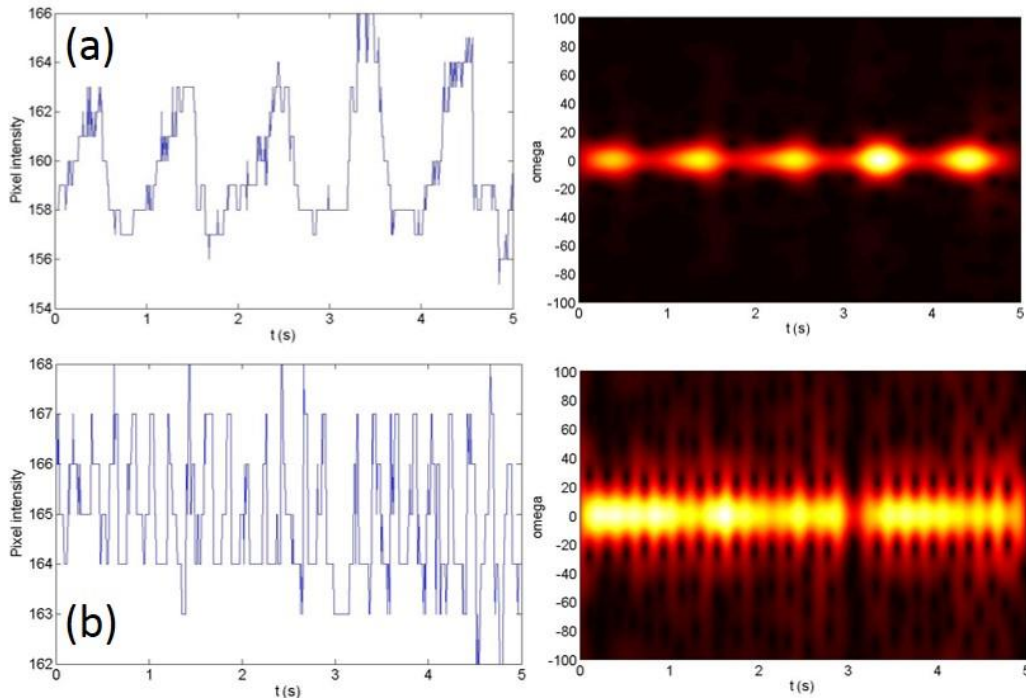


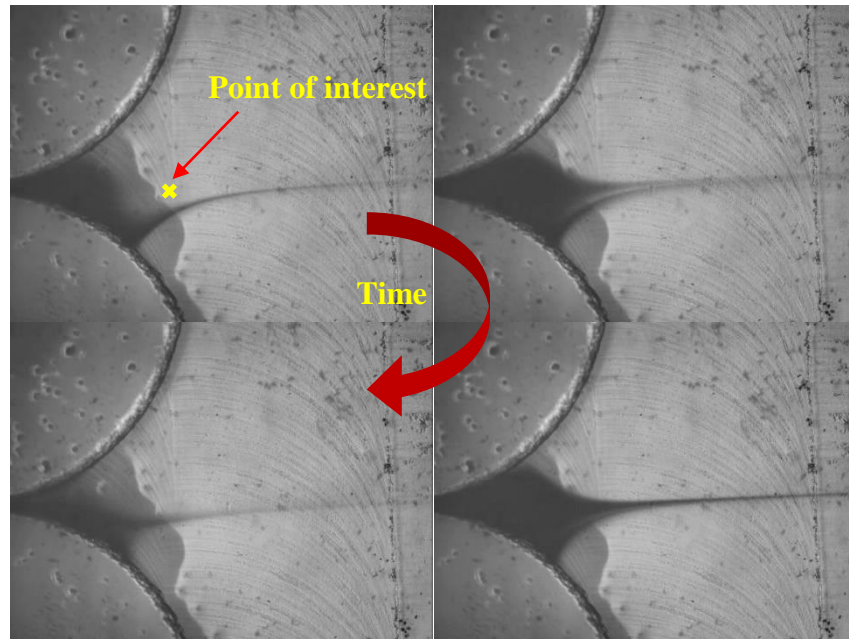
Figure 16: (a) (left) Gray scale intensities versus time for the case when a 1 Hz voltage signal is

applied to the piezoelectric bender. (a) (Right) a corresponding spectrogram showing distribution of frequencies in the frequency and time domain. (b) (Left) Gray scale intensities versus time for the case when a 5 Hz voltage signal is supplied. (a) (Right) Corresponding spectrogram depicting frequency distribution in the frequency space and time domain. (Appendix E)

Since the 100  $\mu\text{m}$  nozzle in the earlier experiments was fabricated using a 3.175 mm mill bit, it can be postulated that the vicinity of the nozzle's exit hampers the necessary fluid dynamics required to break the plume of dye into individual parcels. Therefore, the mold was reconstructed, but with the addition of 500  $\mu\text{m}$  mill bit to reduce the curvature of the vicinity of the nozzle-exit. This was done to allow for sufficient back-flow - during the relaxation period of the piezoelectric bender – to break the chemical plume into a packet. Moreover, this time instead of using a cellophane sheet, PMMA blocks and clamps to seal the device, a thin layer of PDMS was cured on the channel-side of the device. A piece of double-sided tape was then used to mount the piezoelectric bender atop the PDMS membrane. The design alteration eventually reduced complexity.

For the new series of experiments ink was filled into the chamber and the piezoelectric transducer was actuated using a square wave signal and a specified duty cycle. The latter was done so that the effects of the negative pressure sucking the liquid back into the chamber could be attenuated. Figure 17 (a) portrays a series of images showing time-wise variation in the concentration of ink around the point of interest (yellow marker). Analysis was done to determine temporal variation in the dye concentration about the point of interest (Figure 17 (b)). The graph shows approximately square wave behaviour of ink concentration in time.

(a)



(b)

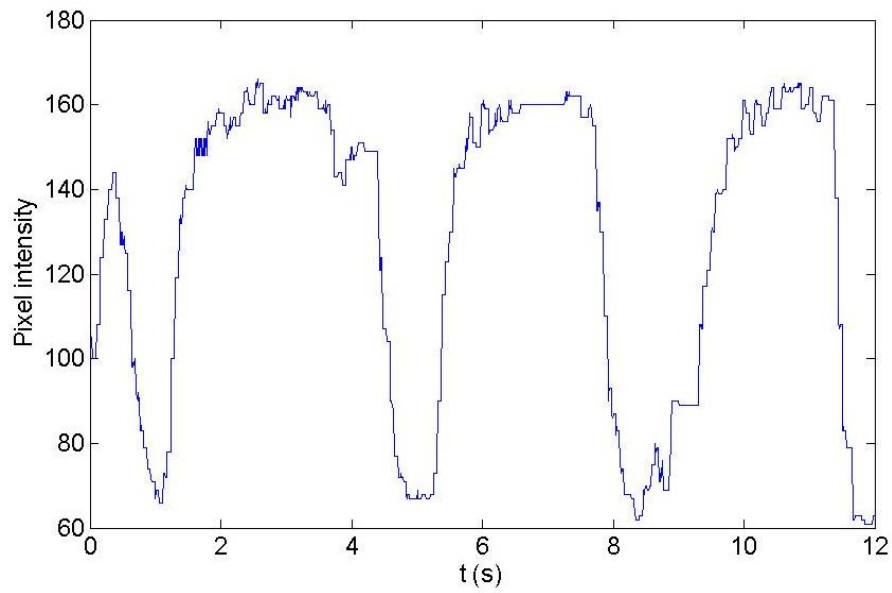


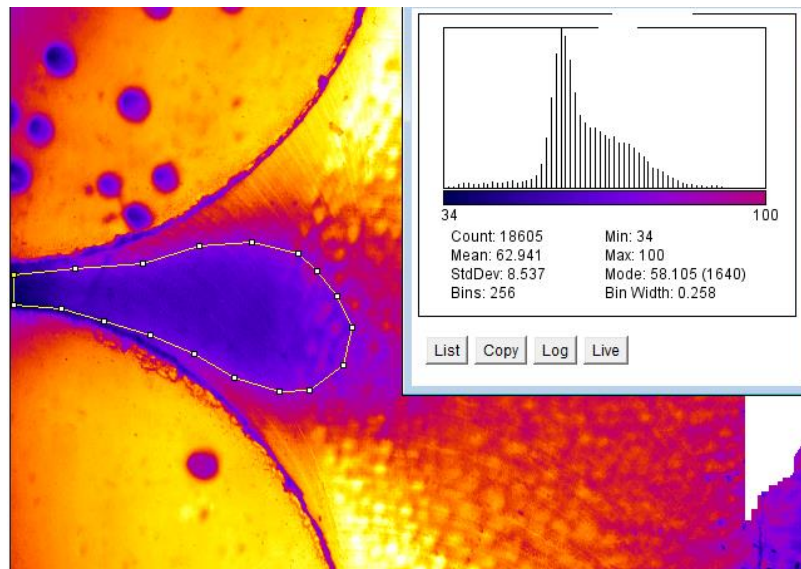
Figure 17: (a) the sequence of images show a time-wise variation in the colour of the dye stream at a given point of interest (marked in yellow). (b) Similar values of maximum and minimum

pixel intensities over a considerable period suggest a stable temporal concentration gradient.

Although a concentration gradient was established, individual chemical packets could still not be dispensed. The shear stress from the incoming flow of DI water causes the chemical plume to squish and flow. This implies that for a system of two miscible liquids - with a negligible surface tension difference – flows at low Re number will render the dispensing of individual chemical packets extremely challenging.

Keeping this into account, the flow of DI water to the inlets of the T-channel was cut-off in a different set of experiments. As a consequence a spatiotemporally varying chemical plume was observed. For the case when a 1 Hz square voltage signal with 50 % duty cycle was applied, the chemical plume was pulled back into the reservoir due to negative pressure during relaxation period of the piezoelectric bender. The frames of the recorded videos were analyzed using Image-J; a thermal filter was applied to make the plume more visible. An estimate of the pixel count was obtained for the contraction and dilatation phase of the chamber (Figure 18 (a) and (b) respectively).

(a)



(b)

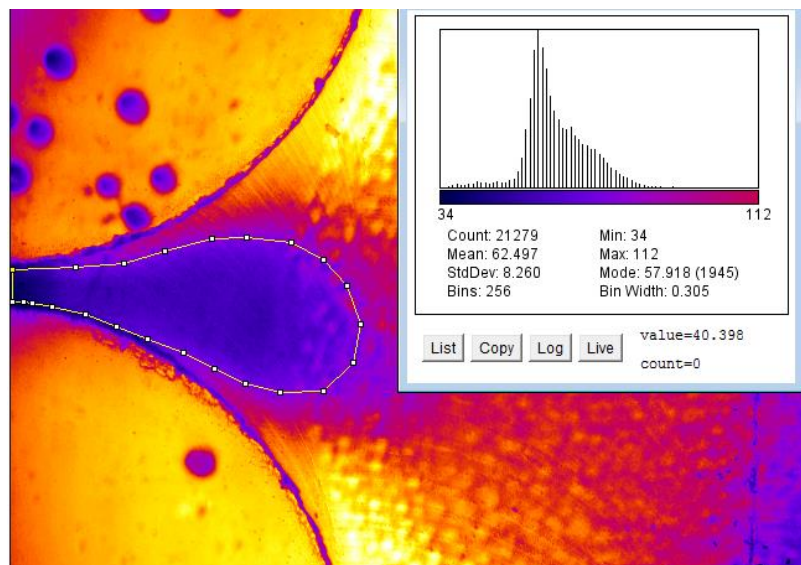


Figure 18: an estimate on the number of pixels making up the plume structure is obtained for two consecutive dilation and expansion cycles. (a) An estimated 18605 pixels enveloping the cloud

of dye is obtained when the piezoelectric bender underwent relaxation and the dye chamber expanded (b) 21279 pixel count is obtained when the chamber underwent compression. Note: at low actuation frequency  $\sim 1$  Hz, an almost constant difference between pixel counts is observed for a considerable duration of device operation.

For low actuation frequency of the piezoelectric transducer, a virtually constant difference between the pixel counts and steady pixel intensities (Figure 19 (a)) over a considerable period of operation was observed. This suggests that for low frequency actuation the device operates reasonably for smaller time duration without undergoing substantial degradation in its efficiency. This can be attributed to diffusion dominated mixing of ink in water. Since the relaxation time of the bender is small, therefore a large proportion of ink molecules do not get sufficient time to travel farther away from the nozzle and escape the region influenced by the negative pressure. Nevertheless, it is observed that the plume eventually grows in size as more and more chemical molecules diffuse outward as time progresses. Moreover, for considerable period of operation water molecules that are pulled into the chamber can alter the concentration of the chemical. At higher actuation frequencies the plume growth is more pronounced (Figure 19 (b)) than at lower actuation frequencies. A significant proportion of ink molecules diffuse outward and some that are pulled back along with water molecules cause the concentration of the plume to change rapidly over small time duration. However, the problem may be overcome if the fluid near the point of interest is constantly refreshed by pumping DI water.



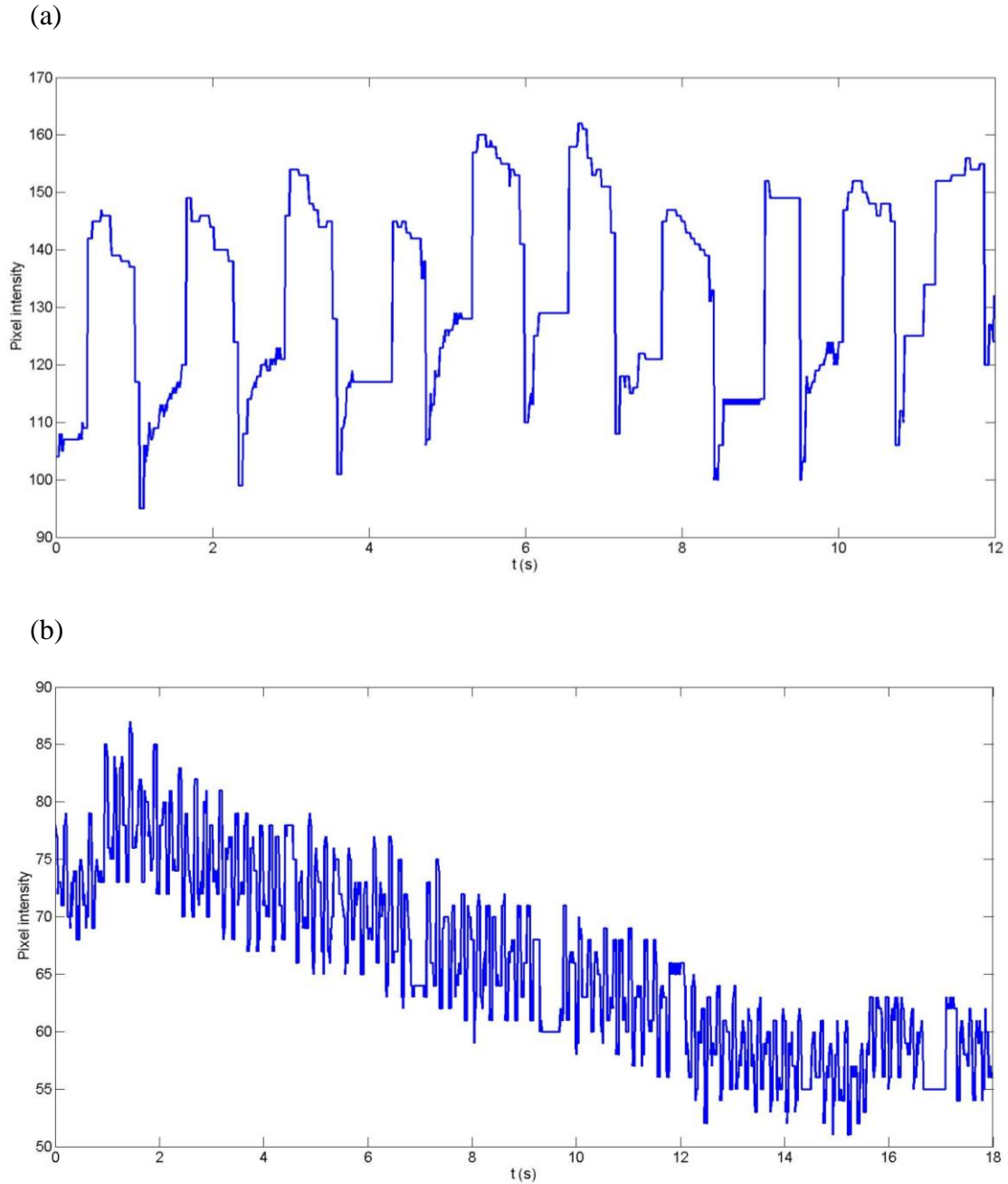


Figure 19: (a) The graph depicts how the pixel intensity changes when a 1 Hz square voltage signal with 50 % duty cycle is applied to the piezoelectric transducer; expansion phase is sudden – pixel intensities fall abruptly – whereas relaxation period is relatively long owing to the 50 % duty cycle as can be seen by a gradual rise in pixel intensity. (b) At higher frequency, 8 Hz with

a 50 % duty cycle, the pixel intensities fall with respect to time as more and more ink is pushed farther away from the nozzle and the point of interest.

Two modifications are apparent from the earlier setups. In the first setup, even though a constant perfusion of DI water exists, the nozzle geometry does not ensure appropriate fluid dynamics to break the continuity of the chemical exiting the fluidic chamber. Due to the shape of the nozzle, water is more likely to enter into the chamber during the retraction phase and thereby alter the chemical concentration for long time duration. In the last setup that we investigated, the growth of the chemical plume and its mixing with the quiescent medium affects the chemical concentration at a given location over time. As a result it is unlikely to sustain a specific concentration profile over long periods of operation. The spatiotemporal concentration is affected by the history of the system. However, it was proposed that a constant perfusion could help resolve the issue. Thus, based upon aforementioned arguments a new system can be developed to 1) ensure constant replenishment of fluid in the channel 2) minimize back-flow to the microfluidic chamber. These can help prevent the system's history from affecting spatiotemporal concentration profiles in the future.

For this purpose, a photomask was designed and the chip design was modified to bear a microfluidic nozzle with a width of 100  $\mu\text{m}$ . A PDMS chip was fabricated using the mold and a 200  $\mu\text{m}$  thick PDMS layer was plasma bonded to seal the microfluidic chamber. A piezoelectric bender was mounted atop the PDMS film using double-sided tape. DI water was allowed to flow through the channel at 0.05 mL/min.

Upon actuating the piezoelectric bender with a 1 Hz sine wave a chemical pulse issued forth from the nozzle and exhausted along with DI water. A brief time lag segregated the individual chemical pulses (as shown in Figure 20). A graph of pixel intensity versus time for the event is plotted in Figure 21 at a specific location. The troughs in the waveform are the instances when the chemical concentration at the given location is 0. Since the concentration of pulses are not influenced by the system's history, thus the pulses obtained using this design iteration may be used reliably in future to stimulate neurons and several other cell types.

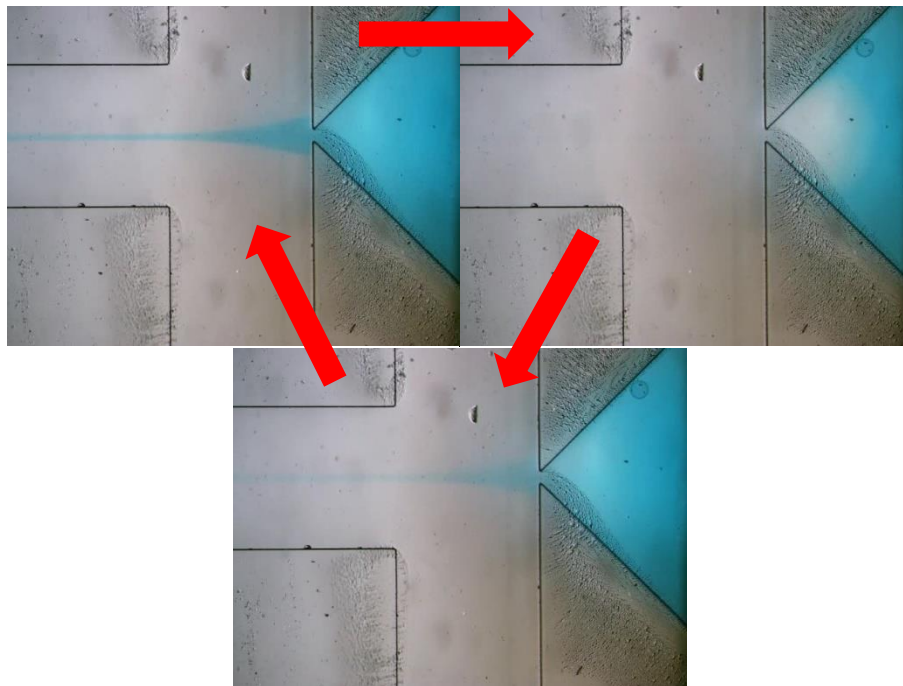


Figure 20: The chemical pulse is released into the channel. The pulse subsides as the piezoelectric bender causes the chamber to expand. A second pulse follows the first one after a brief time lapse.

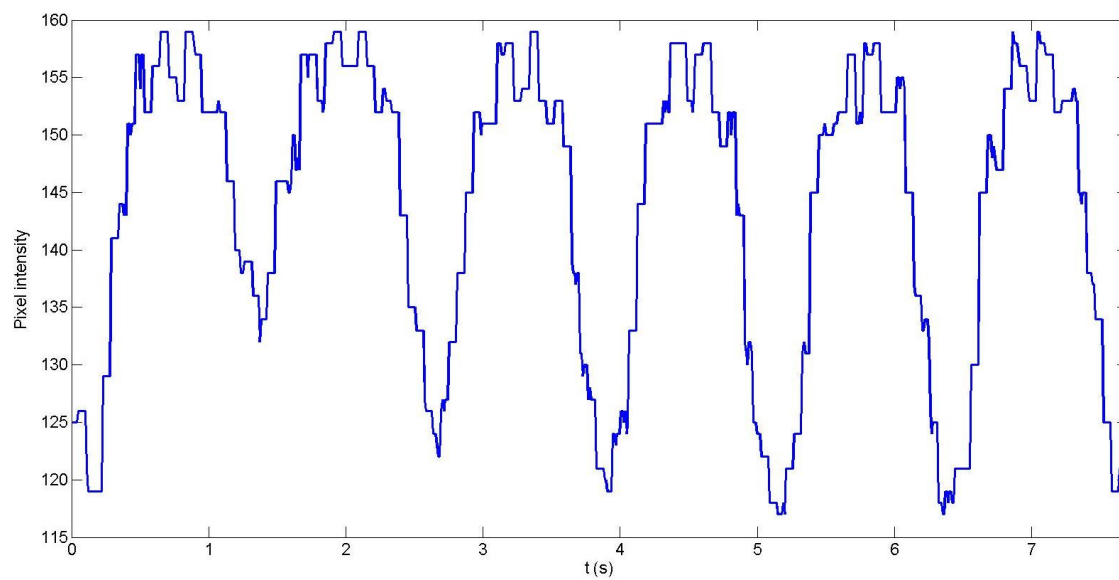


Figure 21: A plot showing pixel intensity versus time for the chemical pulses. A reasonable consistency in waveform can be observed for the duration considered.

## CHAPTER 3 SPATIOTEMPORAL CONCENTRATION CONTROL VIA SYNCHRONIZED PUMPS

### 3.1 Introduction

In the previous chapter, piezoelectric actuation was utilized to generate spatiotemporally varying concentration gradients in a microchannel. However, this particular actuation is not robust since piezoelectric transducers often breakdown after short periods of operation at high voltage settings. There exists a need to seek for relatively more reliable actuation mechanism.

One such method for generating concentration gradients within microchannels involves the usage of coupled syringe pumps. Two syringe pumps can be programmed to work in synchronization such that the analyte concentration can be varied spatiotemporally at a constant total flow-rate. For this to occur, the individual pumps are operated with a phase between them. For instance, Figure 22 is a graphical representation of two synchronized pumps producing a ramp or a triangular concentration signal (the blue line represents the fluid stream with the analyte whereas the green line represents DI water). As delineated by the graph, the sum of the flow-rate of the two fluid streams is a constant at any given instance of time (red line). More complicated signals with various analyte (neurotransmitters, drugs and ions) can be generated by programming the pumps accordingly for a controlled neuronal stimulation. These chemical cues can prove critical for probing neuronal behaviour. For instance,  $\text{Ca}^{2+}$  ions trigger the release of neurotransmitters in a synapse, which makes it interesting to study the effects of varying  $\text{Ca}^{2+}$  concentration on the neuronal firing pattern.

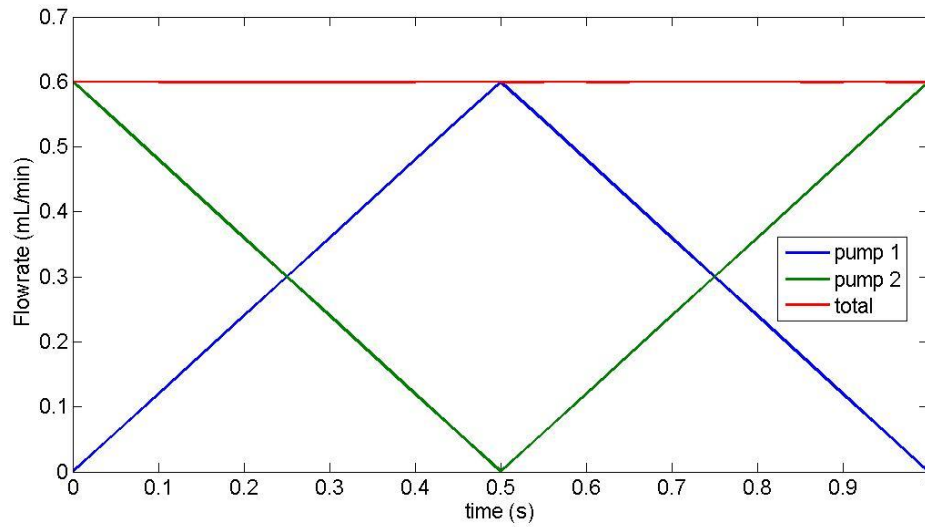


Figure 22: The graph above represents the requisite flow-rate conditions for two fluid streams to generate a ramp concentration waveform. While the fluid stream with the analyte is ramped up (blue), the DI water stream (green) is ramped down generating a triangular concentration profile at a constant total flow-rate (red).

Generating a ramp  $\text{Ca}^{2+}$  ion concentration waveform is non-trivial. Homogeneity of  $\text{Ca}^{2+}$  ions needs to be ensured across the width of the microchannel so that a neuron at a given location bathes and experiences uniform concentration along its length at any given time. However, enhancing mixing in microfluidics has been a long-standing challenge and it comes with the caveat that inertial effects are attenuated and viscous effects are more pronounced for low Re number flows.

### 3.2 Advection

Mixing between two parallel flowing fluid streams in a microchannel is not governed by simple diffusion alone; advection affects diffusion greatly, especially at occasions when Pe number is >

0.1. The entire mixing event can be traced approximately if analytical or numerical solutions to the advection-diffusion equation (9) are known.

$$\frac{\partial C}{\partial t} = \nabla \cdot (D \nabla C) - \nabla \cdot (\vec{v} C) \quad (9)$$

where  $C$  denotes the concentration of species,  $t$  represents time,  $\vec{v}$  denotes the average velocity of the fluid and  $D$  denotes the diffusion coefficient

However, analytical solutions to this differential equation are limited to a few simple cases, for example two streams of fluid flowing parallel to each other with zero relative velocity. In the case of a triangular chemical waveform, the flow rate of the individual fluid streams is changing in time, and thus obtaining analytical solutions with a periodic boundary condition is extremely challenging.

A strong urge to perform simulation for the triangular chemical waveform arises from the notion that some qualitative information regarding the analyte concentration profile can be inferred.

Moreover, some important parameters may be identified prior to conducting experiments.

In order to carry out simulations for the case of interest, the moving boundary conditions were discretized in time and known analytical solutions<sup>51</sup> were utilized to compute the spatiotemporal concentration profiles for the first half-cycle (refer to Appendix F)

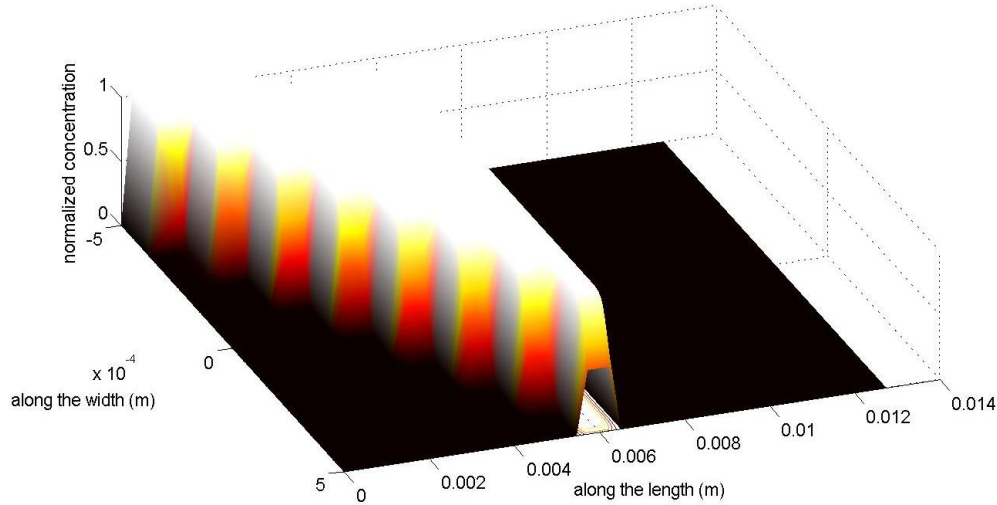


Figure 23: The surface profile depicts the normalized concentration profile of Calcium ions across the length and width of the microchannel (1 mm) during the first 0.5 seconds while the flow-rate of the fluid stream with the analyte molecules is ramped up to a maximum 0.6 mL/min. Owing to a small transverse diffusion coefficient and the duration considered, it can be inferred that the calcium ions will not diffuse significantly across the width of the microchannel.

Figure 23 shows a normalized concentration profile of calcium ions computed for a constant total flow rate of 0.6 mL/min for a period of 0.5 second across a 1mm wide microchannel; the diffusion coefficient of calcium ions is assumed to be  $5.3 \times 10^{-6} \text{ cm}^2/\text{s}^{52}$ . Because of the relatively small coefficient, diffusion in both lateral and transverse direction is suppressed. Furthermore, it is reasonable to assume that for small diffusion coefficients and low Re number ( $\text{Re} \ll 1$ ) the concentration profile will be mirrored during  $t = 0.5 \text{ sec}$  to  $t = 1 \text{ sec}$  - as flow-rate of the calcium ion solution is decreased and that of DI water is increased accordingly. The ramping of flow-rate gives rise to chemical packets which will eventually homogenize for a very long period of time or theoretically for an infinite length of channel.



From simulations we can also infer that the concentration of calcium ions will vary with respect to time at any given location in the channel. To validate this claim, for instance, the diffusion coefficient can be increased arbitrarily to induce some degree of enhanced artificial mixing for the first-half cycle. The diffusion coefficient was increased to  $5.3 \times 10^{-6} \text{ m}^2/\text{s}$  and simulations were performed to determine the concentration of  $\text{Ca}^{2+}$  ions. A location on the centreline of the T-channel, at a distance of 2.86 mm from the inlet was selected – also an arbitrary choice – to determine the concentrations at two different time intervals.

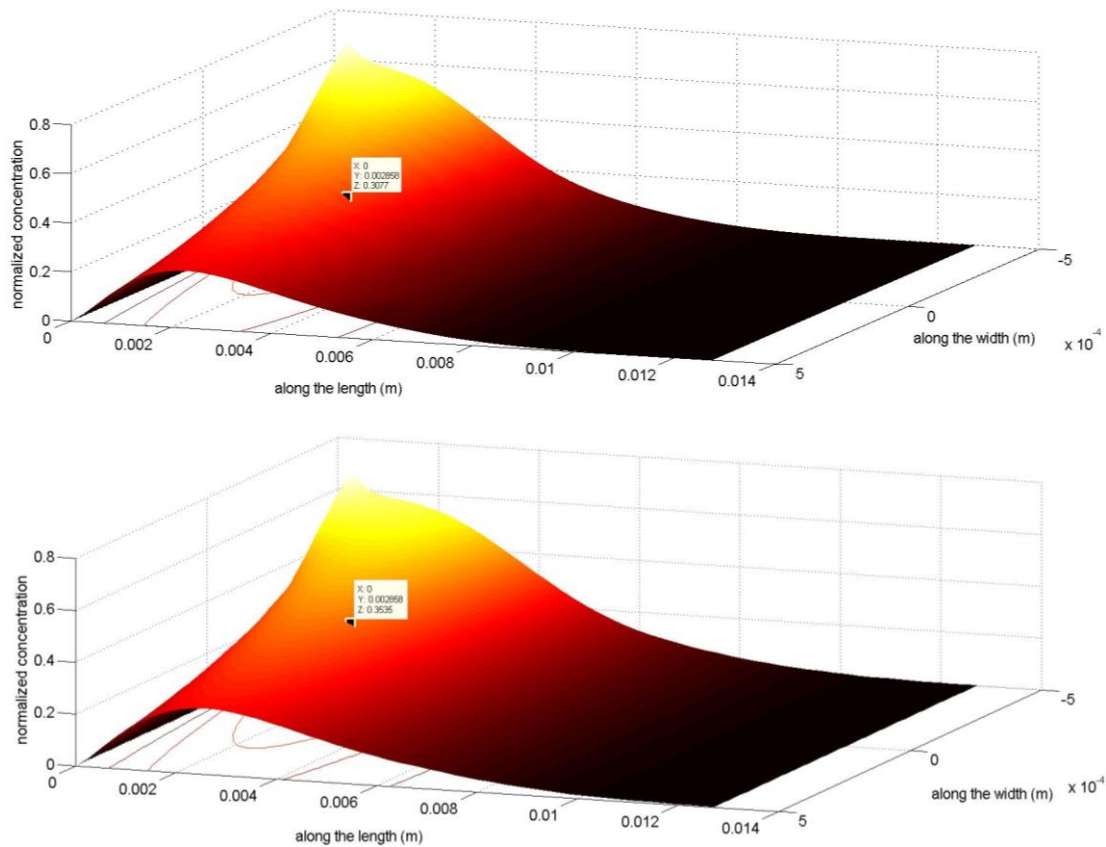


Figure 24: The surfaces delineate normalized concentration profiles at two different time instances with artificial diffusion coefficients and the markers show the normalized concentration in the middle of the channel at a distance of 2.86 mm from the entrance: (top

image) a normalized concentration of 0.3077 at 0.4 sec (bottom) a normalized concentration of 0.3535 at  $t = 0.5$  sec.

As can be seen from the two profiles (Figure 24), the normalized concentration of ions at the designated location is 0.3077 at  $t = 0.4$  sec and increases to 0.3535 at  $t = 0.5$  sec. With passage of time the ramping of flow rate will displace the interface between the fluid streams and cause the concentration of calcium ions to increase/decrease periodically.

Nevertheless, it is necessary to state that the simulations performed above are a very crude quantitative measure of the analyte distribution obtained for the first half of the pump cycle. Besides idealized assumptions, one of the major limitations in solving the diffusion-advection equation for the case at hand is the extent to which the boundary conditions are discretized.

### **3.3 Setup Validation**

With a qualitative measure of analyte distribution the next phase is to experimentally obtain a ramp concentration profile with calcium ions. Two NE1000X programmable pumps were utilized for the purpose. A simple program was used to configure the two pumps. A critical problem, prior to working with the calcium ion solution, is to ensure whether the pumps could actually be used in conjunction to yield a ramp concentration waveform. Note that calcium ion solution cannot be used for making this check as it is transparent in nature. Techniques do exist wherein optical methods can be utilized for imaging calcium ion concentration, such as using calcium indicators<sup>53</sup>. But simple optical measurements, that involve visual observation under an ordinary light microscope, would require at least one of the solutions to be coloured.

So, in lieu of calcium ion solution a quick check can be performed with a dye to observe the generation of triangular waveforms and test the performance of the two pumps.

A  $7.92 \times 10^{-4}$  molar solution of Erioglaucine di-sodium salt was pumped into a 1 mm wide T-channel along with a stream of DI water. In order to ensure proper mixing, the two fluid streams were allowed to mix via a Y-connector. After exiting the Y-connector, the two streams were allowed to mix along an 8 cm length of tubing before entering the microfluidic channel. The pumps were programmed to maintain a constant total flow-rate of 0.6 mL/min – such that the conditions provided in Figure 22 were met - while enabling the generation of a ramp chemical signal. Videos recordings were analyzed to obtain the spatiotemporal concentration gradient of Erioglaucine di-sodium salt (Figure 25). A noticeable feature of the graph is the shape of the chemical signal that to a reasonable extent resembles a ramp/triangular waveform.

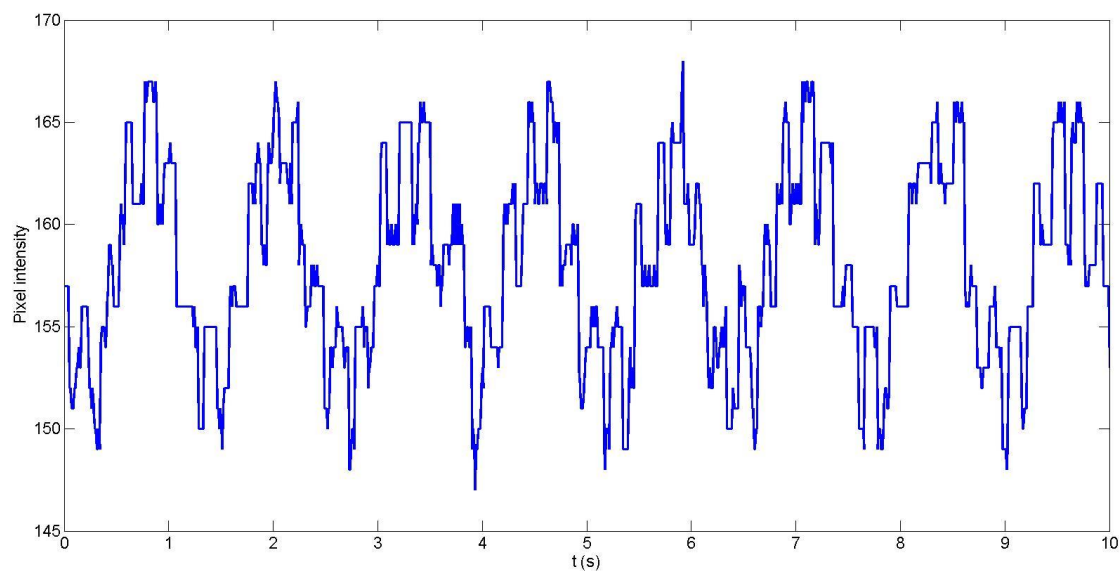


Figure 25: The graph represents the change in pixel intensity as the local concentration of

Erioglaucine di-sodium salt varies across the width of the microchannel. The intensity variation can be used indirectly to infer information for the analyte. The chemical waveform is approximately triangular which is in accordance with the expectation. Higher frequencies in the signal may be due to rapid fluctuations in the light settings.

Regression analysis (Appendix G) can be performed to analyze the extent to which the chemical waveform conforms to a triangular wave. For the purpose, the interval for the first peak is selected and a piece-wise linear function (solid lines) for fitting the data (dots) is determined using the methods of least squares (see Figure 26). A 7.2 % deviation between the magnitudes of the two gradients and an average  $R^2$  value of 0.744 implies that it is reasonable to assume a symmetric ramp-like behaviour for the chemical signal.

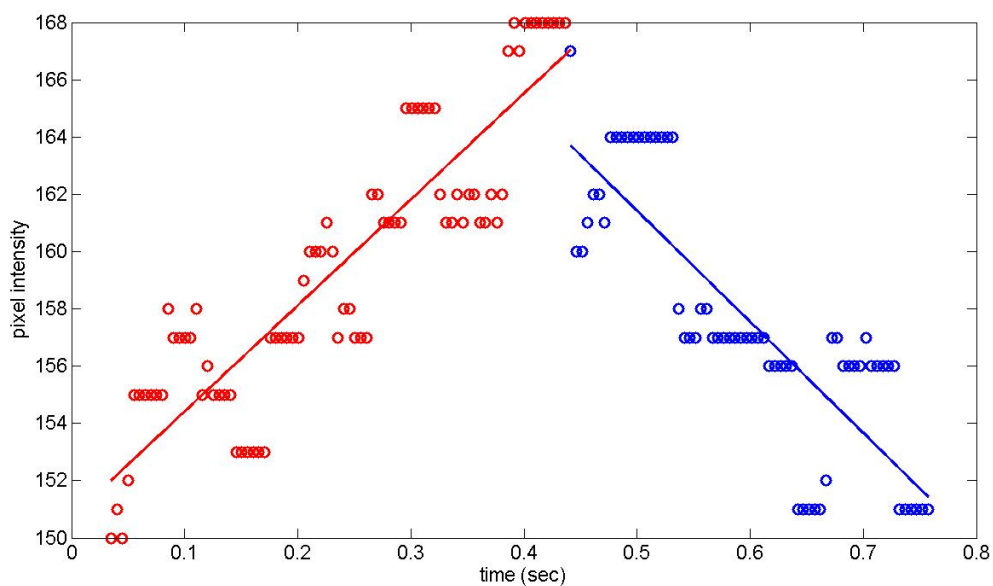


Figure 26: Method of least squares is used to determine the extent to which the chemical waveform conforms to a ramp/triangular shape. The gradients of 37.00 and -38.79 as well as an

average  $R^2$  value of 0.744 suggest it is reasonable to assume a triangular waveform.

Similarly a sine-regression analysis yields an  $R^2$  value of 0.702 (Figure 27). A sinusoidal fit can be deemed as physically more realistic since the pumps cannot have an infinite acceleration.

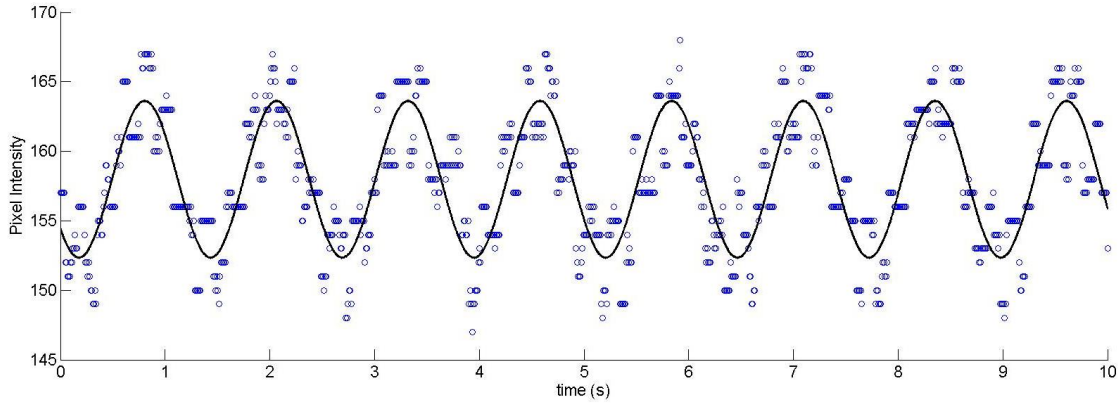


Figure 27: A sinusoidal regression of the same data set (as in Figure 25) results in an  $R^2$  value of 0.702. A sinusoidal fit is more realistic because the pumps cannot have an infinite acceleration.

### 3.4 Device fabrication

With validation of our current setup the final stage was to generate the calcium ion concentration gradients within the microchannel. A special chip was designed to detect the calcium ion concentration. The microfluidic device is based on a recently reported lab-on-a-chip system, which is fabricated with standard lithography and bonding methods<sup>54,55</sup>. In the fabrication process, a silicon wafer serves as the substrate and is cut into  $2\text{ cm} \times 3\text{ cm}$  pieces with a dicing saw machine. Multi-teeth electrodes with a  $5\text{ }\mu\text{m}$  gap are used to ensure the controlled Dielectrophoresis (DEP) alignment of nano sensors. The electrodes are fabricated by patterning metal layers of Cr and Au on the silicon wafer surface through metal sputtering, optical lithography, and wet etching. Then a negative photoresist SU-8 3050 is spin-coated on the Si

surface as the second layer which contains all the microfluidic components. The predesigned microchannels are transferred from the photomask to the SU-8 layer with UV lithography. The protected SU-8 layer under the photomask is dissolved in the SU-8 developer, leaving only the exposed, cross-linked SU-8 structure which encloses the micro-channel network used in the device. The final step is bonding a piece of PDMS to SU-8 to form a sealed channel. Surface treatment is necessary in the bonding step. Oxygen plasma and 5% 3-aminopropyltriethoxysilane (APTES) solution are used for the SU-8 surface treatment which introduces amine ( $\text{Si-NH}_2$ ) groups on the surface. For PDMS, oxygen plasma is used to generate silanol ( $\text{Si-OH}$ ) groups. The covalent bonds of  $\text{Si-O-Si}$  formed by amine and silanol chemical groups bond the SU-8 and PDMS tightly. The lab-on-a-chip system with predesigned microfluidic structures can precisely control the fluids in our system. The schematic structure of the microfluidic device is illustrated in Figure 28 (a) and the actual fabricated device is shown in Figure 28 (b). The device, slightly larger than a dime, consists of an inlet, outlet, a microfluidic channel, and an electrode array with integrated nano sensors. It was fabricated to experimentally test the performance of the ion sensors.

Recently, different types of concentration sensors have been developed using various principles. For example, microfluidic systems based on enzyme assays have been developed for the in-channel detection of glycerol<sup>56</sup> but such devices are complicated and are only applicable for certain temperature ranges. However for the fluorescence sensors, the need of specialized instruments, the use of a high-intensity light, and the limited spatial resolution limit their accessibility for a routine laboratory usage. These limitations along with complex testing

procedures make such systems incompatible with microfluidic systems for on-site chemical concentration sensing. Electrochemical sensors might prove a better candidate since they have simple structures which can be integrated easily and effectively with the microfluidic platforms.

Calcium sensors have been investigated previously using various approaches. Among them, ion-selective electrodes have proven to be an effective method for calcium detection<sup>57,58</sup>. Membranes inside these electrodes allow calcium ions to pass through for selective detection. In addition, such calcium sensors have been successfully integrated into microfluidic devices for real-time detection<sup>58</sup>. In this work, we use a configuration with *p*-type single-walled carbon nanotubes (SWCNTs) as the integrated nano sensors similar to a previously reported microfluidic system<sup>59</sup>.

SWCNTs have attracted significant attention in many areas, especially in the biomedical and chemical fields, due to their extraordinary electrical and mechanical properties<sup>60</sup>. Previous studies show that the aqueous ionic density<sup>61</sup> and flow velocity<sup>62</sup> can influence SWCNT-based sensors since they have high sensitivity towards the electric potential caused by the specific binding and unbinding effects between ions and SWCNTs in a microfluidic environment. SWCNT-based devices provide a label-free, real-time, and ultrasensitive approach for sensing applications<sup>63</sup>. Based on the well-developed microfabrication technology, the SWCNT sensors can be fabricated with smaller size and more uniform geometry for a more reliable performance than their counterparts. They have been used in a wide range of micro/nanoscale sensing applications, for instance, sensing shear stress<sup>64</sup> and chemical concentration<sup>65</sup>.

Being extremely small, it is nearly impossible to align SWCNTs using mechanical methods. The SWCNTs are deposited along electrodes using a technique known as Dielectrophoresis (DEP). In it, a variable potential difference (an AC voltage source) applied across a pair of metal electrodes generates a non-uniform electric field which exerts a force, termed as the di-electrophoretic force  $F_{DEP}$  (10), on the particles in its vicinity. The force then acts upon the particles and causes them to align inside the electric field.

$$F_{DEP} = \frac{\pi r^2 l}{3} \epsilon_m \operatorname{Re} \left\{ \frac{\epsilon_p^* - \epsilon_m^*}{\epsilon_m^*} \right\} \nabla |\vec{E}_{rms}|^2 \quad (10)$$

where  $r$  and  $l$  denotes the radius and the length of the particle respectively,  $\epsilon$  represents permittivity with subscript  $m$  and  $p$  designating the medium and the particle respectively. The ‘\*’ superscript denotes complex permittivity and  $\nabla |\vec{E}_{rms}|^2$  is square of the gradient of electric field strength.

For DEP, the device was firstly mounted on a probe station (Signatone S1160) and a signal generator was used to supply a 5 MHz 10 V<sub>pp</sub> sinusoidal wave across the metal electrodes. The inlet of the microfluidic channel was connected to a syringe containing approximately 0.2 mg/mL CNT solution. The solution was injected into the channel for approximately 40 seconds during which the V<sub>rms</sub> was observed to drop from ~ 9.1 V to ~ 7.4 V. With subsequent withdrawal of the CNT solution from the channel the V<sub>rms</sub> was observed to drop considerably to ~ 5.4 V. Voltage drop during the process indicates that the DEP was performed successfully.



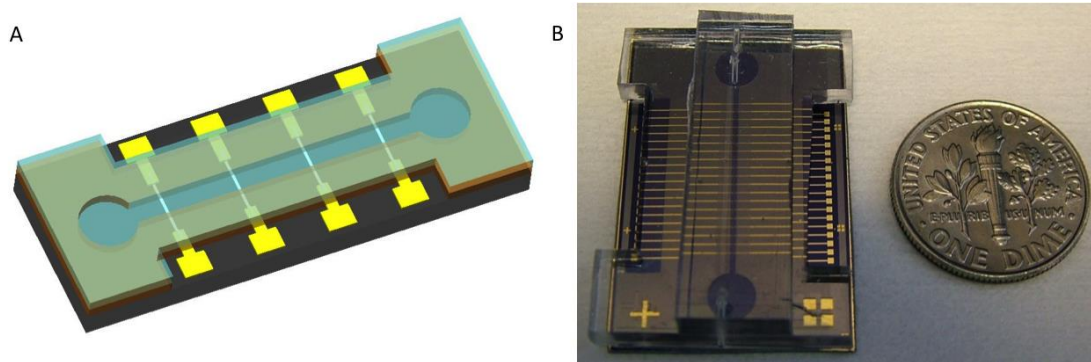


Figure 28: (a) Schematic of the device (b) actual device used for sensing  $\text{Ca}^{2+}$  ion concentration gradients in a microchannel. The device – comparable in size to a dime - comprises of a 1 mm wide channel and houses electrodes along which SWCNTs are deposited.

### 3.5 Experimental results

Figure 29 shows the experimental test rig that was utilized to generate the calcium ion concentration gradients in the microfluidic device. Specific and repeatable signals can then be used to stimulate neurons; this will be briefly touched upon in the concluding chapter. Two NE 1000 X syringe pumps are programmed to maintain a constant total flow-rate of 0.3 mL/min while the flow rate of the individual fluid streams are ramped up and down at 1 Hz.

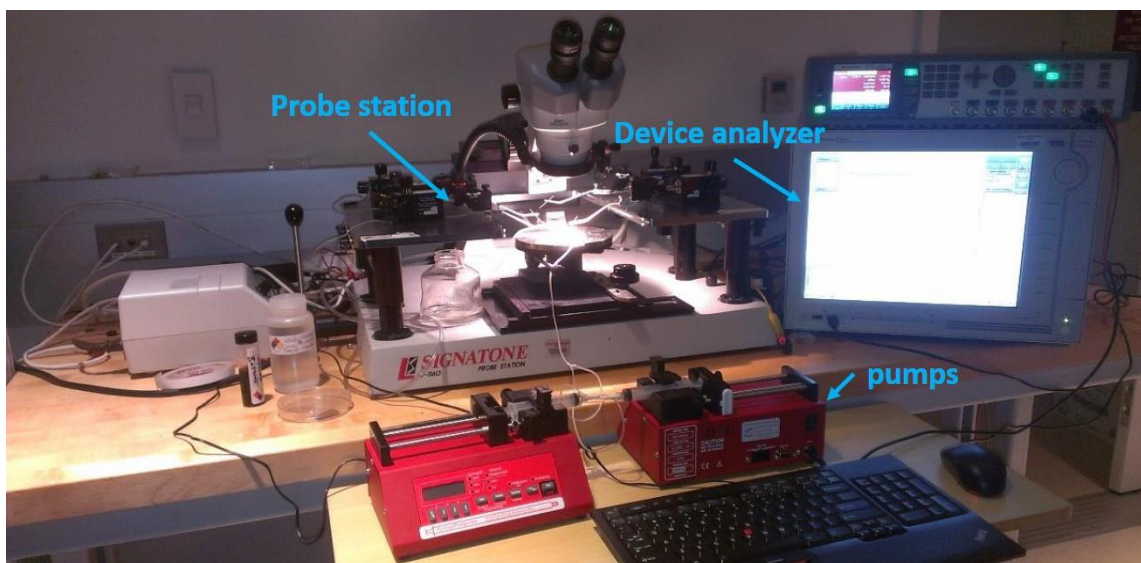


Figure 29: The image shows the experimental setup: two NE 1000X programmable syringe pumps are used to ramp and dispense Calcium ion solution and DI water into the microchannel. A probe station connected to a semiconductor device analyzer is used to collect the current from the CNT sensors and display a resistance time graph.

One of the two 10 mL syringes is filled with DI water and the second with a 10 mM aqueous solution of calcium chloride. A Y-connector is used to connect the two syringes together and a sufficiently long length of tubing allows for pre-mixing to occur between the two fluids before the fluid stream enters the microchannel.

A semiconductor device analyzer (Agilent B1500A) connected to the probe station is used to apply a constant 5 V across the carbon nanotubes deposited between pairs of oppositely facing electrodes. The device analyzer collects the current as the concentration of  $\text{Ca}^{2+}$  ions varies temporally. The current is subsequently used to obtain a resistance-time graph. The current or

resistance-time graph in essence provides a measure of the local variation in  $\text{Ca}^{2+}$  ion concentration. In the experiments, the data was sampled with a sampling rate of 20 ms. Furthermore, a filter was applied to smoothen the sampling over the power line cycle during analog-to-digital conversion.

Figure 30 shows the resistance versus time graph obtained for the stated experimental conditions. As can be seen, the frequency of resistance change of CNTs is  $\sim 1$  Hz and agrees well with the expected frequency of the change in the  $\text{Ca}^{2+}$  ion concentration. In our experiments, the nanosensors' resistance varies periodically as the  $\text{Ca}^{2+}$  concentration in the aqueous solution changes. The observed trend could be explained by the electrokinetic theory of the adsorbed  $\text{Ca}^{2+}$  ions on the surface of the SWCNTs. An earlier study<sup>59</sup> with p-type SWCNTs demonstrate that positive ends of polar molecules serve as a gate voltage for the SWCNTs. Since our SWCNTs are p-type, therefore an increase in  $\text{Ca}^{2+}$  concentration will likely deplete p-doping<sup>54</sup> in the SWCNTs and increase the resistance of the nanosensors, and vice versa. However, it has to be noted that the sensing mechanisms of nanoscale materials could be very complicated due to many other effects, such as the effects from the substrate, Schottky barrier, gate capacitance, and carrier mobility<sup>66,67</sup>.

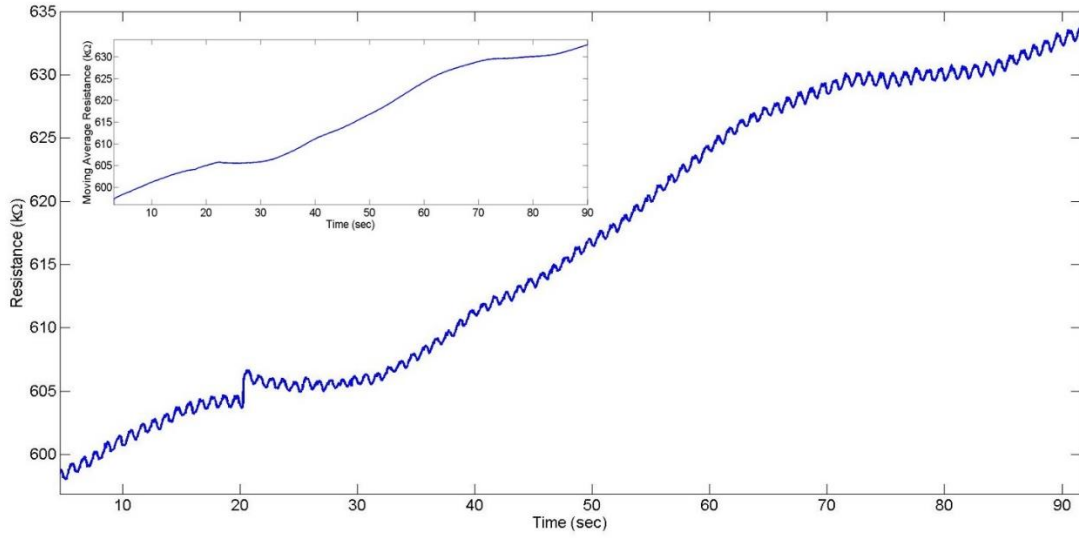


Figure 30: The curve shows the resistance change of CNTs during a 90 sec operation. The periodic fluctuation in the resistance change is  $\sim 1$  Hz. A bias can be detected due to which the average of the resistance change steps up in time. The inset shows the moving average in the resistance change.

A Fourier Transform is performed to determine the frequency distribution in the signal. As delineated by Figure 31, the amplitude for the expected frequency of 1 Hz is relatively larger compared to higher frequencies. The trend displays that any contribution from frequencies greater than 5 Hz is almost negligible. As a corollary, the distribution implies that no extra filtering mechanism is required.

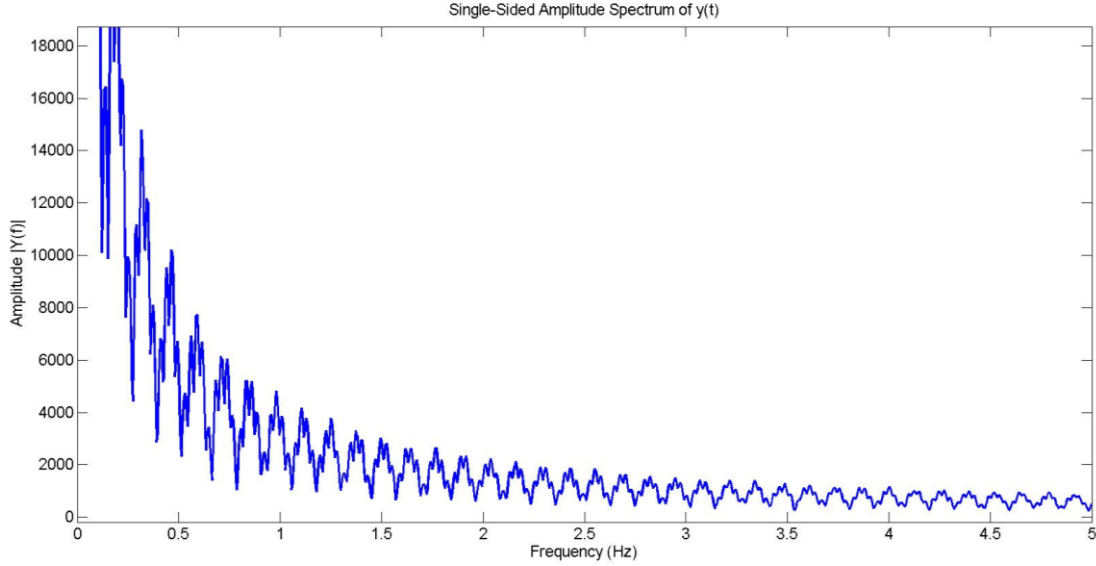


Figure 31: The graph shows the single sided frequency distribution of the signal. Amplitude for frequencies lower than 5 Hz, especially 1 Hz is relatively larger compared to higher frequencies, which implies that no extra filtering is needed. (Refer to Appendix H)

Nevertheless, there is an unexpected bias in the original signal owing to which the average resistance moves up in time (inset of Figure 30). This may be attributed to temporal fluctuations in the flow as the pumps undergo stepping, temperature gradients within the fluid stream or perhaps thermal dissipation within the SWCNTs. Another reason for the observable bias maybe the reversible/irreversible bending, torsion, kinking of SWCNT in response to the flow<sup>68</sup>. Bending or twisting of SWCNT can lower the transmission function and leads to an increase in resistance.

The moving average in the original signal can be compensated for by passing the signal through a filter. The filtered signal (shown in Figure 32) is distributed across a common reference i.e. 0.

Note that the filtered signal no longer displays the resistance change about a true value. In fact, it only depicts the relative resistance change. The signal can however be calibrated to provide a quantitative measure of the variation in  $\text{Ca}^{2+}$  ion concentration in the flow.

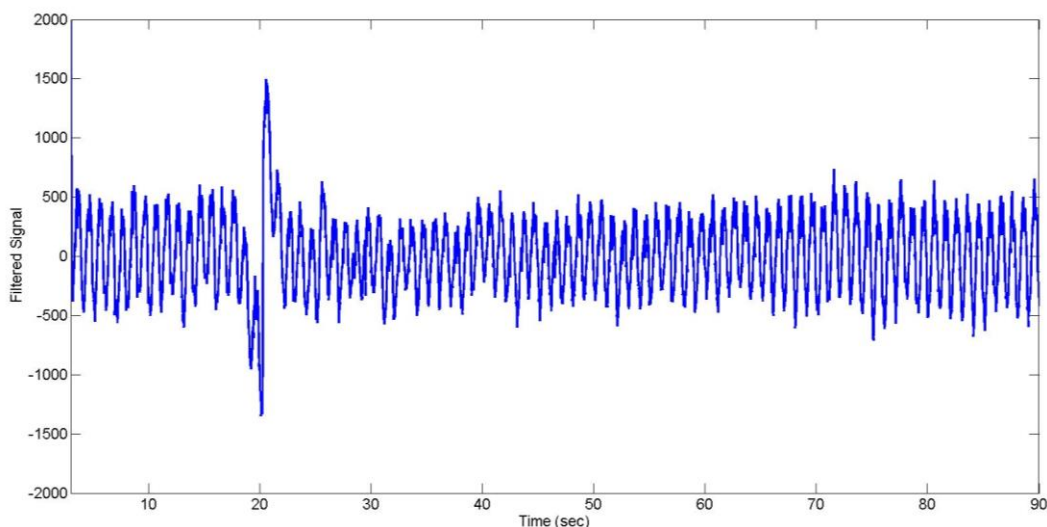


Figure 32: The filtered signal, corrected for the moving average, shows the relative change in resistance of the CNTs. (Appendix I)

In this chapter a couple of programmable pumps were exploited to generate concentration gradient using calcium ions in a microfluidic device. SWCNTs were used as nanosensors for detecting temporal profile of chemical waveform in the microchannel. The method was sought as an alternative to piezoelectric transducers and was employed primarily owing to its robustness. However, the pumps are incapable of yielding high actuation frequencies due to a limit on the stepping of the motor driving the pump shaft.

## CHAPTER 4 CONCLUSION AND FUTURE PERSPECTIVES

### 4.1 Summary

Chemical stimulation of neurons and various cell types - with which neurons interact – has been largely ignored in the neuroscience community. The primary reason is that precise chemical concentration control is hard to attain on a macroscopic scale. Microfluidics can be used to bridge the gap. Special platforms can be developed that can enable chemical stimulation of neurons starting from a few Hz to approximately 1 kHz. These can then be used to test the effects of various drugs over a long period of time and the imbalances in neurotransmitter concentration at a time-scale on the same order as the action potential.

Two different methods were explored to generate concentration gradients within microchannels. The first method involved usage of piezoelectric transducers to compress and decompress a PDMS based microfluidic chamber. The second method involved the use of two synchronized syringe pumps for generating chemical waveforms while maintaining a constant total flow-rate.

Using the method of piezoelectric actuation a number of different chemical switches and their variants were developed. The devices were used to generate chemical waveforms with frequencies exceeding slightly above 5 Hz. Results show that the piezoelectric method requires significant improvement for producing chemical signals at higher actuation frequencies.

The primary issue is lack of one-to-one motion correspondence between the PDMS and the

transducer. The PDMS films - onto which the piezoelectric transducers are mounted - experience relaxation on a time-scale that ranges from 10 milliseconds to approximately 10 seconds<sup>69</sup>. In such systems we observe that at actuation frequencies beyond 10-1000 Hz the PDMS piece does not move in synchronization with the piezoelectric transducer, implying that the system behaves as a damped system with a phase shift – with the effect exacerbating at higher actuation frequencies. It is perhaps that hysteretic damping causes substantial dissipation of power within the polymer.

There are a number of other issues that are problematic: piezoelectric benders produce a noticeable displacement only at higher voltage settings, which poses an extreme hazard. For long periods of operation, cracks tend to develop on the surface of the piezoelectric bender due to mechanical deformation of thin ceramic films. This causes the charge to leak across the width of the bender causing short-circuiting. Moreover, with passage of time, the natural degradation of the brittle ceramic films causes attenuation in the blocking force and the free displacement of the bender. Furthermore, the difficulty of device fabrication with piezoelectric actuation is another critical issue that needs to be addressed.

In crux, the inability to maintain a desirable waveform for longer time durations and breakdown at higher voltage settings render the current piezoelectric benders unsuitable for generating concentration gradients reliably.

There was a need to seek for a more robust method to generate chemical waveforms in a microchannel for the purpose of stimulating a neuron and/or neuronal networks. Thus, a second



method was exploited for its robustness. Two syringe pumps were synchronized in such a way that a triangular chemical waveform was generated at a constant total flow-rate. A triangular chemical waveform with  $\text{Ca}^{2+}$  ions was reliably obtained at a frequency of 1 Hz for a long period of operation, albeit higher frequencies cannot be attained using mechanical pumps. The primary issue is that there is a limit on the stepping time of the motors driving the pump. Mechanical pumps, e.g. NE 1000X used in this study, cannot be used to generate chemical waveforms with time-periods smaller than a second.

A secondary issue with mechanical pumps involves constantly programming the pumps. Unlike piezoelectric actuators, programming the pumps usually cannot be done in real-time to produce requisite shapes of chemical signals with desirable frequencies. A tertiary issue is to ensure homogeneous mixing between the fluids before the stream approaches the region of interest. The latter can be achieved quite conveniently by incorporating a small mixing mechanism into the setup.

Based on the methods investigated, the author is of the opinion that piezoelectric benders coupled with polymeric devices alone are insufficient for generating rapid chemical signals in microchannels. On the other hand, mechanical pumps alone, although extremely sturdy for long periods of operation, cannot be used to yield chemical waveforms at higher frequencies.

Nevertheless, some improvement might be possible for the two setups: for instance, a rigorous experimentation can be performed to change the composition of PDMS as well as the geometry

of the device to decrease the relaxation time of PDMS to a minimum. With a relaxation time on the order of a few milliseconds, it should be possible to obtain an actuation of up to 1 KHz.

Moreover, piezoelectric benders with a higher blocking force and free deflection - at low voltages - can be potentially used. For the second method, pumps with a lower stepping period can be utilized. Also, a proper mixing mechanism needs to be installed after the Y-connector to ensure homogeneous mixing of fluids across the width of the channel.

A union of piezoelectric transducers and pumps seems to be one of the ways via which chemical waveforms at higher actuation frequencies and time durations can be attained. Two piezoelectric pumps can be used in conjunction to produce a desirable chemical signal. The pumps can be programmed in real-time with ease merely by supplying the correct voltage and frequency setting.

## **4.2 Future perspectives**

A feedback loop can be constructed in future to establish a novel dynamic clamp method. The original dynamic clamp technique uses a real-time electrical interface between living cells and neural simulations in order to investigate hypotheses about neural function and structure<sup>70,71</sup>. It has been used successfully to dissection the functionality of single neurons and small neural circuits. However, it has two major drawbacks<sup>72</sup>: the electrodes can clamp electrically only a small section of a cell, and hence frequently do not control the behavior of whole cells; and all control to-date has been concentrated on the electric properties of neurons, neglecting their chemical state. As noted<sup>72</sup>, the latter has been done by necessity, since until recently registering

or controlling the chemical state of either neurons or the chemical environment in which they reside has been essentially impossible with the level of precision needed to simulate the appropriate dynamics of the various extracellular chemical players.

As an extension of this study and with a reliable control over chemical concentration the author believes that the following feedback loop can be generated to study the response of neurons as well as other cell bodies with which neurons interact (Figure 33): an input chemical cue will be supplied by the piezoelectric pumps to the chemical switch. A feedback loop with amplifier ( $A_1$ ) and attenuator ( $K_1$ ) will be used to monitor the  $Ca^{2+}$  ion concentration and ensure that the desirable concentration scheme is met. The input will be used to stimulate a cell body (which may be any cell type that interacts with a neuron). The response of the cell ( $E_{o2}$ ) will be determined. The signal will be converted using an operator and fed to a mathematical model (an artificial neuron), such as the Hodgkin-Huxley model, which will eventually affect the input signal by altering the working of the pumps to generate a signal specific to the neuronal response.

With such a versatile platform for the neuroscience community, it is hoped that both the neuronal interactions as well as the interaction of neurons with other cell types can be understood in a more comprehensive way. Furthermore, it is hoped that this feedback mechanism will be the first step toward understanding the effects of anomalous chemical stimulation and its possible relation to diseases such as Parkinson's disease. Moreover, the platform may provide essential cues for developing a brain on a chip in the near future.

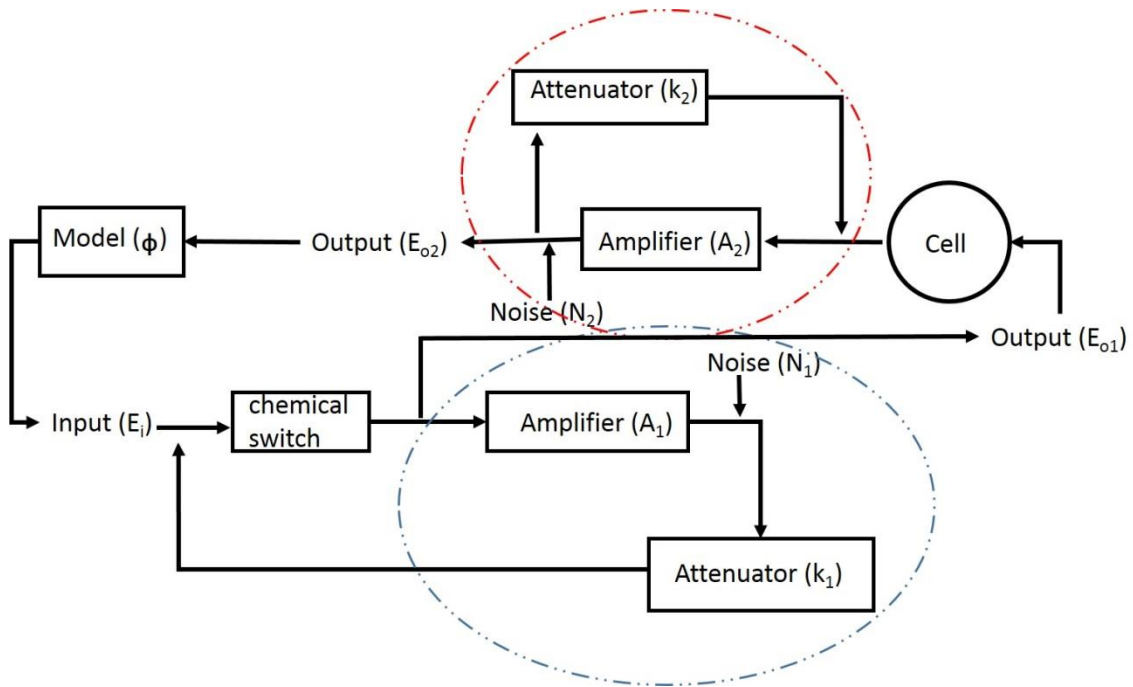


Figure 33: Proposed dynamic clamp feedback loop for neurochemical modulation. A chemical input is supplied to a cell and its response is fed to a mathematical model which affects the input chemical concentration akin to a live neuron.

## APPENDIX

### Appendix A: Code for diffusion across fluid-fluid interface

```
close all; clear all; clc;

N=100; % initializing a scalar

t = linspace(0,10000,N); % introducing time-steps

width = 4e-3; % width of the straight-section of the T-channel

x1n = linspace(-width/2,0,N); x1 = x1n(1:N); % discretizing half-width of the channel with
analyte solution

x2n = linspace(0,width/2,N); x2 = x2n(1:N); % discretizing the second half of the channel

x = [x1,x2]; % concatenating the discretized halves of the channel width

D_a = 7.5e-10; % initializing the diffusion constant of analyte (glutamate)

c_1 = zeros(length(t),length(x)); % initializing a matrix for storage of concentration

for i=1:length(t)

    for j=1:length(x1)

        c_1(i,j) = (1-(0.5*(1+ erf(x(j)./(2.*(D_a^0.5).*(t(i).^0.5)))))); % computing spatio-
temporal concentration for one-half

    end

    for j=length(x1):length(x)

        c_1(i,j) = 0.5*(erfc(x(j)./(2.*(D_a^0.5).*(t(i).^0.5)))); % spatiotemporal conc. for second-half

    end

end

end
```

```
plot(x,c_1(:,:), 'Linewidth',1) % plots dimensionless analyte concentration along the width of  
the channel as fluid parcels move in time  
  
title('Normalized Glutamate Spatiotemporal Concentration Profiles') % adds title to the plot  
  
xlabel('Position (m)') % adds label to the x-axis  
  
ylabel('Dimensionless concentration (C_x/C_o)') % adds label to the y-axis
```

## Appendix B: Histograms for pixel intensity at different flow conditions

% Code for plotting histogram for pixel intensity at various flow-rates

```
clear all; close all; clc;
```

```
n = 3; % initializing a scalar representing the images to be analyzed
```

```
jj = 1; % initializing the counter
```

```
figure; % creates a figure
```

```
while jj <= n
```

```
eval(['image_input = imread("C:\Users\user\Desktop\thesis\Spatial Mixing\spatial  
mixing\matlab\' num2str(jj) '.tif');']) % inputs ...
```

```
% sequence of images in Matlab
```

```
gray_image = rgb2gray(image_input); % converts RGB image to grayscale
```

```
cropped_gray_image = imcrop(gray_image,[700 0 1400 1920]); % automatically crops the  
image according to [x y width height]
```

```
imhist(cropped_gray_image); % plots the histogram of pixel intensity
```

```
hold on % holds the figure
```

```
jj = jj+1; % raises the counter
```

```
pause(0.1) % adds a delay
```

```
end
```

## Appendix C: Diffusion profile of analyte (experimental)

%% Code for computing concentration profiles

clear all; close all; clc;

matrix\_mean\_pixel\_intensity = []; % creates a null matrix for future data storage and to allow concatenation.

n = 16; % number of images to be analyzed

for jj = 1:1:n

    eval(['image\_input = imread("C:\Users\user\Desktop\thesis\Spatial Mixing\time lapse\'

num2str(jj) '.tif');']) % loads sequence of images

    if jj> 1 && jj<=n

        load matrix\_mean\_pixel\_intensity; % loads mean\_pixel\_intensity.mat

    end

    imshow(image\_input); % displays the input image

    gray\_image = rgb2gray(image\_input); % converts RGB image to grayscale

    figure(2); % creates a separate figure

    cropped\_gray\_image = imcrop(gray\_image, [700 0 1400 1920]); % automatically crops the image according to [x y width height]

    imshow(cropped\_gray\_image); % displays the cropped up image

    [rows columns extraneous]= size(cropped\_gray\_image); % extracta information regarding number of pixels in the cropped image

    line\_divisions = double(cropped\_gray\_image(1:rows,1:columns)); % converts the type of 'cropped\_grayscale\_image' to double



```

mean_pixel_intensity = zeros(rows,1); % initializes a vector for storage of mean pixel intensity
min_I = mean(min(line_divisions)); % finds minimum value of intensity in the image
max_I = mean(max(line_divisions)); % finds maximum value of intensity in the image
del_I = max_I - min_I; % difference between the maximum and the minimum intensities
if del_I ~= 0 % executes command for incomplete mixing
    line_divisions(1:rows,:) = 255*(line_divisions(1:rows,:)- min_I)/(del_I); % scales or stretches
    the pixel intensity on 0-255 scale
    for i = 1:rows
        mean_pixel_intensity(i,1) = mean(line_divisions(i,:)); % computes the mean pixel intensity
    end
elseif del_I == 0 % executes command for zero diffusion-gradient
    mean_pixel_intensity(:,1) = max_I; % set constant intensity for all pixels
end
matrix_mean_pixel_intensity = [matrix_mean_pixel_intensity, mean_pixel_intensity]; %
concatenates mean pixel intensity of multiple images for multiple execution
save matrix_mean_pixel_intensity 'matrix_mean_pixel_intensity'; % saves the vector
'matrix_mean_pixel_intensity'
pause(0.1) % adds delay of 0.1 sec
end

%% Plotting results from previous cell

clear all; close all; clc;

load matrix_mean_pixel_intensity; % loads 'matrix_mean_pixel_intensity'

```

```
S = size(matrix_mean_pixel_intensity);    % records size of matrix_mean_pixel_intensity  
normalized_width = (1:1:S(1))/S(1); % generates normalized width using number of rows of  
pixels  
plot(normalized_width,matrix_mean_pixel_intensity) % generates a plot of pixel intensity along  
the width
```

## Appendix D: Relative mixing index

% Code for calculating relative mixing index for a mixing event from a sequence of images

%% Code for calculating relative mixing index

clear all; close all; clc;

matrix\_rel\_mixing\_index = []; % creates a null matrix for future data storage and to allow concatenation.

n=19; % number of images to be analyzed

for jj = 1:1:n

while jj ~= 1

load matrix\_rel\_mixing\_index; % loads matrix\_rel\_mixing\_index.mat

break

end

eval(['image\_input = imread("D:\research\thesis\mixing index\correct images\nikon\bright\'

num2str(jj) '.tif');']) % loads images from destination folder

% image\_input(:, :, 4) = [];

imshow(image\_input); % displays the input image

gray\_image = rgb2gray(image\_input); % converts RGB image to grayscale

figure(2); % creates a separate figure

cropped\_gray\_image = imcrop(gray\_image,[654.5 83.5 (698-654) (867-83)]); % automatically

crops the image according to [x y width height]

imshow(cropped\_gray\_image); % displays the cropped up image

```

[rows columns extraneous]= size(cropped_gray_image); % extracts information regarding
number of pixels in the cropped image

line_divisions = double(cropped_gray_image(1:rows,1:columns)); % converts the type of
'cropped_grayscale_image' to double

mean_I = mean(line_divisions(:,:)); % computes mean pixel intensities in the selected area

while jj ==1

for j = 1:columns

standard_deviation_not(1,j) = (sum((line_divisions(:,j)-((mean_I(1,j))))).^2))^0.5;

end

standard_deviation_not = mean(standard_deviation_not); % computes original std. deviation

break

end

for j =1:columns

    standard_deviation(1,j) = (sum((line_divisions(:,j)-(mean_I(1,j))))).^2))^0.5;

end

standard_deviation = mean(standard_deviation); % computes local std. deviation

avg_relative_mixing_index = (1- standard_deviation/standard_deviation_not)*100; % yields
relative mixing index from std. deviation

matrix_rel_mixing_index = [matrix_rel_mixing_index, avg_relative_mixing_index]; %
concatenates mixing indices of multiple images for multiple execution

save matrix_rel_mixing_index 'matrix_rel_mixing_index' 'standard_deviation_not' 'n'; % saves
the vector 'matrix_mixing_index' and scalar ' n '

```

```

pause(0.05)

end

%% Plotting and curve-fitting relative mixing indices

close all; clear all; close all

time = [0, 10, 20, 30, 40, 50, 60, 70, 80, 90, 100, 110, 120, 150, 180, 210, 240, 270, 300, 330,
360]; % time elapsed at which images were captured

load matrix_rel_mixing_index; % loads 'matrix_rel_mixing_index'

time = time(1:n);

curve_fit = polyval(polyfit(time,matrix_rel_mixing_index,4),time); % fits a polynomial
through the data

plot(time,matrix_rel_mixing_index,'rs',time, curve_fit,'linewidth',2) % plots experimental data
and curve fits it

xlabel('Time elapsed (sec)'); ylabel('(1 - Relative Mixing Index)*100%');

```

## Appendix E: Concentration profile and spectrogram

%% Code for generating concentration profiles

```
clear all; close all; clc;
```

```
matrix_mean_pixel_intensity = []; % creates a null matrix for future data storage and to allow  
concatenation.
```

```
n = 619; % number of images to be analyzed
```

```
for jj = 1:1:n
```

```
    eval(['image_input = imread("C:\Users\user\Desktop\videocompressed-  
fastchemicalswitch\frames-1Hz\' num2str(jj) '.jpeg");']) % loads sequence of images
```

```
    if jj> 1 && jj<=n
```

```
        load matrix_mean_pixel_intensity; % loads mean_pixel_intensity.mat
```

```
    end
```

```
    imshow(image_input); % displays the input image
```

```
    gray_image = rgb2gray(image_input); % converts RGB image to grayscale
```

```
    figure(2); % creates a separate figure
```

```
    cropped_gray_image = imcrop(gray_image, [251 228 0 0]); % automatically crops the image  
    according to [x y width height]
```

```
    imshow(cropped_gray_image); % displays the cropped up image
```

```
    [rows columns extraneous]= size(cropped_gray_image); % extracts information regarding  
    number of pixels in the cropped image
```

```
    line_divisions = double(cropped_gray_image(1:rows,1:columns)); % converts the type of  
'cropped_grayscale_image' to double
```

```

mean_pixel_intensity = zeros(rows,1); % initializes a vector for storage of mean pixel intensity
for i = 1:rows
    mean_pixel_intensity(i,1) = mean(line_divisions(i,:)); % computes the mean pixel intensity
end

matrix_mean_pixel_intensity = [matrix_mean_pixel_intensity, mean_pixel_intensity]; %
concatenates mean pixel intensity of multiple images for multiple execution

save matrix_mean_pixel_intensity 'matrix_mean_pixel_intensity' 'n'; % saves the vector
'matrix_mean_pixel_intensity' and the scalar 'n'

% pause(0.1) % adds delay of 0.1 sec
end

%% Plotting results from previous cell

clear all; close all; clc;

load matrix_mean_pixel_intensity; % loads 'matrix_mean_pixel_intensity'

S = size(matrix_mean_pixel_intensity); % records size of matrix_mean_pixel_intensity

normalized_width = (1:1:S(1))/S(1); % generates normalized width using number of rows of
pixels

plot((linspace(1,5,n)),(matrix_mean_pixel_intensity(1,:))) % generates a plot of pixel intensity

%% Code for FFT and G-transform for spectrogram

clear all; close all; clc;

load matrix_mean_pixel_intensity; % loads the matrix matrix_mean_pixel_intensity

n = length(matrix_mean_pixel_intensity(1,:))-1;

T = 5; % time for which analysis is performed

```

```

t2 = linspace(0,T,n+1); t = t2(1:n); % time-domain broken down into n pts but since last point
is the same so the point is excluded from t.

k = (2*pi/T)*[0:n/2-1 -n/2:-1]; ks = fftshift(k); % wave number 'k' and its shift 'ks'

S_local = matrix_mean_pixel_intensity(1,1:end-1);

S_min = min(matrix_mean_pixel_intensity(1,1:end-1));

S_max = max(matrix_mean_pixel_intensity(1,1:end-1));

S = (S_local - S_min)/(S_max - S_min);

St= fft(S); % Fourier transform of signal

width = 25; % width of filter

slide = linspace(0,5,n); % resolution in time for sliding window

spec = []; % add a null matrix

for j=1:length(slide)

    f = exp(-width*(t-slide(j)).^2); % filter moving in time

    Sf = f.*S; %filtered signal (multiplying filter with signal)

    Sft = fft(Sf); % Fourier transform of filtered signal

    subplot(3,1,1), plot(t,S,'k',t,f,'m'), title('original signal with a moving filter')

    subplot(3,1,2), plot(t,Sf,'k'), title('filtered signal')

    subplot(3,1,3), plot(ks, abs(fftshift(Sft)/max(abs(fftshift(Sft))))), title('the transform') %

normalized plotting

axis([-80 80 0 1])

drawnow

pause(0.01)

```



```

spec = [spec; abs(fftshift(Sft))];    % adding rows in a matrix without having to override the
previous value to plot a spectrogram

end

figure(2)

pcolor(slide,ks,spec.',shading interp % plotting the spectrogram

set(gca, 'Ylim', [-100 100], 'FontSize', [14])

colormap(hot)

xlabel('t')

ylabel('omega')

figure (3)

plot(ks, abs(fftshift(St))/max(abs(fftshift(St))))

```

## Appendix F: Solution of diffusion advection equation for half-cycle of the pumps

```
%% solution to diffusion advection equation for half cycle

clear all; close all; clc;

flow_rate = 0.6*1.666667e-8; % total flowrate

diameter_tubing = 1e-3; width = 1e-3; % diameter and width of the tubing

area = pi*(diameter_tubing^2)/4; % area of tubing

u = flow_rate/area; % average fluid velocity

del_t = 1; % time for one complete pump cycle

distance = u*del_t; % displacement of fluid

D_l = 5.3e-6; % lateral diffusion coefficient of fluid

D_t = D_l;

M = 50; % Discretization of T-channel in x-y axis

x = linspace(0,distance,M);

y = -width/2:width/100:width/2;

T = 0.5; n = T/8; % Discretization of time

t1 = 0:n:T/2; t1(1) = 0.0000001;

t2 = T/2:n:T;

t = [t1, t2];

a = linspace(0,0.5,5).*width; % equation parameter

concentration = zeros(length(x),length(y)); % matrix to store normalized concentration

format long
```

```

for k = 1:length(t1)-1

    for i=1:length(x)

        for j =1:length(y)

            func = @(ti)x(i)./((16*pi*D_1)^0.5).*(ti.^-1.5).*erfc((a(end-
k)+y(j))./(4*D_t*ti).^0.5)).*exp(-((x(i)-u.*ti)./(4*D_1*ti).^0.5)).^2);

            concentration(i,j,k) = integral(func,t1(k),t1(k+1));

        end

    end

end

for k=1:length(t2)-1

    for i=1:length(x)

        for j =1:length(y)

            func = @(ti)x(i)./((16*pi*D_1)^0.5).*(ti.^-
1.5).*(erf((a(end)+y(j))./(4*D_t*ti).^0.5)+erf((a(k+1)-y(j))./(4*D_t*ti).^0.5)).*exp(-((x(i)-
u.*ti)./(4*D_1*ti).^0.5)).^2);

            concentration(i,j,4+k) = integral(func,t2(k),t2(k+1));

        end

    end

end

[W,L] = meshgrid(y,x);      % meshing the grid in x and y direction

sum = 0;

```

```

for l = 1:2*k

sum = sum + concentration(:,l);    % summing concentration due to superposition

end

surf(W,L,sum), shading interp, colormap(hot), xlabel('along the width (m)'), ylabel('along the
length (m)'), zlabel('normalized concentration')    % generating surface profile

```

## Appendix G: Regression analysis (linear and sinusoidal fit)

% least squares fit to chemical waveform

clear all; close all; clc;

load matrix\_mean\_pixel\_intensity.mat % loads 'matrix\_mean\_pixel\_intensity'

time = linspace(0,5,n); % total duration of the signal

join = [(1:n);time; matrix\_mean\_pixel\_intensity]'; % matches pixel intensity with time

y1 = join(8:89,3); % first half of the 1st peak is isolated

t1 = join(8:89,2); % duration for the first half of the 1st peak

y2 = join(89:152,3); % second half of the 1st peak is isolated

t2 = join(89:152,2); % duration for the second half of the 1st peak

plot(t1,y1,'rs', t2,y2,'bs'); xlabel('time (sec)'); ylabel('pixel intensity') % data points are plotted for the first peak

hold on

p1 = polyfit(t1,y1,1);p2 = polyfit(t2,y2,1); % linear fit to the two halves of the peak

plot(t1,polyval(p1,t1),'r', t2, polyval(p2,t2),'b'); % plotting the linear fits

SSE = sum((y1 - (p1(1)\*t1 + p1(2))).^2);

SSY = sum((y1 - mean(y1)).^2);

SSE2 = sum((y2 - (p2(1)\*t2 + p2(2))).^2);

SSY2 = sum((y2 - mean(y2)).^2);

R\_squared1 = 1 - SSE/SSY; % R\_squared for the first linear fit

R\_squared2 = 1 - SSE2/SSY2; % R\_squared for the second linear fit

R\_squared\_avg = 0.5\*(R\_squared1 + R\_squared2); % average R\_squared value

```
%% sinusoidal fit to chemical waveform
```

```
scatter(linspace(0,10,n), matrix_mean_pixel_intensity) % plotting the data points for the  
signal
```

```
hold on
```

```
B0 = mean(matrix_mean_pixel_intensity); % vertical shift
```

```
B1 = (max(matrix_mean_pixel_intensity(1,:)) - min(matrix_mean_pixel_intensity(1,:)))/2; %  
amplitude
```

```
B2 = 5; % phase (number of peaks)
```

```
B3 = 0; % phase shift (eyeball the Curve)
```

```
myFit = NonLinearModel.fit(linspace(0,10,n),matrix_mean_pixel_intensity, 'y ~ b0 +  
b1*sin(b2*x1 + b3)', [B0, B1, B2, B3]) % sinusoidal fit to the data. Note that all the coefficient  
estimates are very good except for b3 where any even integer is equally valid
```

```
%% look at the complete set of methods
```

```
methods(myFit)
```

```
%% Generate a plot
```

```
hold on
```

```
plot(linspace(0,10,n), myFit.Fitted)
```

```
hold off
```

## Appendix H: Fourier transform of signal

```
% single-sided amplitude spectrum.

L= size(signal,1);    % length of matrix, signal = [time, resistance];

Fs = 50;             % sampling rate in Hz

y = electrode80(:,2); % resistance;

NFFT = 2^nextpow2(L); % Next power of 2 from length of y

Y = fft(y,NFFT)/L;

f = Fs/2*linspace(0,1,NFFT/2+1);

plot(f,2*abs(Y(1:NFFT/2+1))) % plot of single-sided amplitude spectrum

title('Single-Sided Amplitude Spectrum of y(t)')

xlabel('Frequency (Hz)')

ylabel('|Y(f)|')
```

## Appendix I: Filter for moving average

```
% filtering moving averages.

Fs=50;             % sample rate in Hz

window = 4;        % window size for filter

B = ones(1,Fs*window)/Fs/window;

delay = round((Fs*window-1)/2);

electrodenoshift = filter(B,1,[electrode80(:,2); zeros(delay,1)]);

ensnd = electrodenoshift( (delay+1):end ); % removal of moving average

plot(electrode80(:,1),electrode80(:,2)/10^3); xlabel('time (s)'); ylabel('Resistance (kOhm)')
```

```
figure(2)
```

```
plot(electrode80(:,1),ensnd/10^3); xlabel('time (s)'); ylabel('Average resistance (kOhm)')
```

```
figure(3)
```

```
plot(electrode80(:,1),electrode80(:,2)-ensnd); xlabel('time (s)'); ylabel('Filtered signal')
```



## BIBLIOGRAPHY

- 1 Shieh, M. C. a. J. C. *Guide to Research Techniques in Neuroscience*. (Academic Press, 2009).
- 2 Sakmann, B. & Neher, E. Patch Clamp Techniques for Studying Ionic Channels in Excitable-Membranes. *Annu Rev Physiol* **46**, 455-472 (1984).
- 3 Squires, T. M. & Quake, S. R. Microfluidics: Fluid physics at the nanoliter scale. *Rev Mod Phys* **77**, 977-1026, doi:DOI 10.1103/RevModPhys.77.977 (2005).
- 4 Xu, J. & Attinger, D. Drop on demand in a microfluidic chip. *J Micromech Microeng* **18**, doi:Artn 065020  
Doi 10.1088/0960-1317/18/6/065020 (2008).
- 5 Wang, J. *et al.* Microfluidics: A new cosset for neurobiology. *Lab on a Chip* **9**, 644-652, doi:10.1039/B813495B (2009).
- 6 Weibel, D. B. & Whitesides, G. M. Applications of microfluidics in chemical biology. *Current Opinion in Chemical Biology* **10**, 584-591, doi:<http://dx.doi.org/10.1016/j.cbpa.2006.10.016> (2006).
- 7 Dittrich, P. S. & Manz, A. Lab-on-a-chip: microfluidics in drug discovery. *Nat Rev Drug Discov* **5**, 210-218 (2006).
- 8 Barry, R. & Ivanov, D. Microfluidics in biotechnology. *Journal of Nanobiotechnology* **2**, 2 (2004).
- 9 Beebe, D. J., Mensing, G. A. & Walker, G. M. PHYSICS AND APPLICATIONS OF MICROFLUIDICS IN BIOLOGY. *Annual Review of Biomedical Engineering* **4**, 261-286, doi:doi:10.1146/annurev.bioeng.4.112601.125916 (2002).

- 10 Whitesides, G. M. The origins and the future of microfluidics. *Nature* **442**, 368-373 (2006).
- 11 Thorsen, T., Maerkl, S. J. & Quake, S. R. Microfluidic Large-Scale Integration. *Science* **298**, 580-584, doi:10.1126/science.1076996 (2002).
- 12 Hong, J. W. & Quake, S. R. Integrated nanoliter systems. *Nat Biotech* **21**, 1179-1183 (2003).
- 13 Stone, H. A., Stroock, A. D. & Ajdari, A. ENGINEERING FLOWS IN SMALL DEVICES. *Annual Review of Fluid Mechanics* **36**, 381-411, doi:doi:10.1146/annurev.fluid.36.050802.122124 (2004).
- 14 Stirman, J. N. *et al.* Real-time multimodal optical control of neurons and muscles in freely behaving *Caenorhabditis elegans*. *Nat Meth* **8**, 153-158, doi:<http://www.nature.com/nmeth/journal/v8/n2/abs/nmeth.1555.html#supplementary-information> (2011).
- 15 Stirman, J. N., Brauner, M., Gottschalk, A. & Lu, H. High-throughput study of synaptic transmission at the neuromuscular junction enabled by optogenetics and microfluidics. *J Neurosci Meth* **191**, 90-93, doi:DOI 10.1016/j.jneumeth.2010.05.019 (2010).
- 16 Ben-Yakar, A., Chronis, N. & Lu, H. Microfluidics for the analysis of behavior, nerve regeneration, and neural cell biology in *C. elegans*. *Current Opinion in Neurobiology* **19**, 561-567, doi:<http://dx.doi.org/10.1016/j.conb.2009.10.010> (2009).
- 17 Caceres, I. D., Valmas, N., Hilliard, M. A. & Lu, H. Laterally Orienting *C. elegans* Using Geometry at Microscale for High-Throughput Visual Screens in Neurodegeneration and Neuronal Development Studies. *Plos One* **7**, doi:ARTN e35037

DOI 10.1371/journal.pone.0035037 (2012).

- 18 Keenan, T. M. *et al.* Automated identification of axonal growth cones in time-lapse image sequences. *J Neurosci Meth* **151**, 232-238, doi:DOI 10.1016/j.jneumeth.2005.07.010 (2006).
- 19 Tourovskaia, A., Figueroa-Masot, X. & Folch, A. Long-term microfluidic cultures of myotube microarrays for high-throughput focal stimulation. *Nature Protocols* **1**, 1092-1104, doi:DOI 10.1038/nprot.2006.123 (2006).
- 20 Park, J., Koito, H., Li, J. R. & Han, A. Multi-compartment neuron-glia co-culture platform for localized CNS axon-glia interaction study. *Lab on a Chip* **12**, 3296-3304, doi:Doi 10.1039/C2lc40303j (2012).
- 21 Taylor, A. M. *et al.* A microfluidic culture platform for CNS axonal injury, regeneration and transport. *Nat Methods* **2**, 599-605, doi:Doi 10.1038/Nmeth777 (2005).
- 22 Figueroa, X. A., Cooksey, G. A., Votaw, S. V., Horowitz, L. F. & Folch, A. Large-scale investigation of the olfactory receptor space using a microfluidic microwell array. *Lab on a Chip* **10**, 1120-1127, doi:Doi 10.1039/B920585c (2010).
- 23 Taylor, A. M. *et al.* A microfluidic culture platform for CNS axonal injury, regeneration and transport. *Nat Meth* **2**, 599-605, doi:[http://www.nature.com/nmeth/journal/v2/n8/supinfo/nmeth777\\_S1.html](http://www.nature.com/nmeth/journal/v2/n8/supinfo/nmeth777_S1.html) (2005).
- 24 Tourovskaia, A., Li, N. Z. & Folch, A. Localized acetylcholine receptor clustering dynamics in response to microfluidic focal stimulation with agrin. *Biophys J* **95**, 3009-3016, doi:DOI 10.1529/biophysj.107.128173 (2008).

- 25 Cooksey, G. A., Sip, C. G. & Folch, A. A multi-purpose microfluidic perfusion system with combinatorial choice of inputs, mixtures, gradient patterns, and flow rates. *Lab on a Chip* **9**, 417-426, doi:Doi 10.1039/B806803h (2009).
- 26 Keenan, T. M. & Folch, A. Biomolecular gradients in cell culture systems. *Lab on a Chip* **8**, 34-57, doi:Doi 10.1039/B711887b (2008).
- 27 Bhattacharjee, N., Li, N., Keenan, T. M. & Folch, A. A neuron-benign microfluidic gradient generator for studying the response of mammalian neurons towards axon guidance factors. *Integrative Biology* **2**, 669-679, doi:10.1039/C0IB00038H (2010).
- 28 Keenan, T. M., Hsu, C.-H. & Folch, A. Microfluidic “jets” for generating steady-state gradients of soluble molecules on open surfaces. *Appl Phys Lett* **89**, -, doi:doi:<http://dx.doi.org/10.1063/1.2345914> (2006).
- 29 Tourovskaia, A., Kosar, T. F. & Folch, A. Local Induction of Acetylcholine Receptor Clustering in Myotube Cultures Using Microfluidic Application of Agrin. *Biophys J* **90**, 2192-2198, doi:<http://dx.doi.org/10.1529/biophysj.105.074864> (2006).
- 30 Botzolakakis, E. J. *et al.* Achieving synaptically relevant pulses of neurotransmitter using PDMS microfluidics. *J Neurosci Meth* **177**, 294-302, doi:<http://dx.doi.org/10.1016/j.jneumeth.2008.10.014> (2009).
- 31 Ventriglia, F. & Di Maio, V. A Brownian model of glutamate diffusion in excitatory synapses of hippocampus. *Biosystems* **58**, 67-74, doi:Doi 10.1016/S0303-2647(00)00108-8 (2000).
- 32 Lee, C. Y., Chang, C. L., Wang, Y. N. & Fu, L. M. Microfluidic Mixing: A Review. *Int J Mol Sci* **12**, 3263-3287, doi:Doi 10.3390/Ijms12053263 (2011).

- 33 Nguyen, N. T. & Wu, Z. G. Micromixers - a review. *J Micromech Microeng* **15**, R1-R16, doi:Doi 10.1088/0960-1317/15/2/R01 (2005).
- 34 Liu, R. H. *et al.* Passive mixing in a three-dimensional serpentine microchannel. *J Microelectromech S* **9**, 190-197, doi:Doi 10.1109/84.846699 (2000).
- 35 Stroock, A. D. *et al.* Chaotic mixer for microchannels. *Science* **295**, 647-651, doi:DOI 10.1126/science.1066238 (2002).
- 36 Park, S. J. *et al.* Rapid three-dimensional passive rotation micromixer using the breakup process. *J Micromech Microeng* **14**, 6-14, doi:Pii S0960-1317(04)58782-X  
Doi 10.1088/0960-1317/14/1/302 (2004).
- 37 Stoeber, B., Liepmann, D. & Muller, S. J. Strategy for active mixing in microdevices. *Physical Review E* **75**, 066314 (2007).
- 38 Li, Y., Zhang, D. L., Feng, X. J., Xu, Y. Z. & Liu, B. F. A microsecond microfluidic mixer for characterizing fast biochemical reactions. *Talanta* **88**, 175-180, doi:DOI 10.1016/j.talanta.2011.10.028 (2012).
- 39 Li, Y., Xu, Y. Z., Feng, X. J. & Liu, B. F. A Rapid Microfluidic Mixer for High-Viscosity Fluids To Track Ultrafast Early Folding Kinetics of G-Quadruplex under Molecular Crowding Conditions. *Analytical Chemistry* **84**, 9025-9032, doi:Doi 10.1021/Ac301864r (2012).
- 40 Garstecki, P., Fischbach, M. A. & Whitesides, G. M. Design for mixing using bubbles in branched microfluidic channels. *Appl Phys Lett* **86**, doi:Artn 244108  
Doi 10.1063/1.1946902 (2005).

- 41 Garstecki, P., Fuerstman, M. J., Fischbach, M. A., Sia, S. K. & Whitesides, G. M. Mixing with bubbles: a practical technology for use with portable microfluidic devices. *Lab on a Chip* **6**, 207-212, doi:Doi 10.1039/B510843h (2006).
- 42 Huang, P. H. *et al.* An acoustofluidic micromixer based on oscillating sidewall sharp-edges. *Lab on a Chip* **13**, 3847-3852, doi:Doi 10.1039/C3lc50568e (2013).
- 43 Mao, X. L., Juluri, B. K., Lapsley, M. I., Stratton, Z. S. & Huang, T. J. Milliseconds microfluidic chaotic bubble mixer. *Microfluidics and Nanofluidics* **8**, 139-144, doi:DOI 10.1007/s10404-009-0496-4 (2010).
- 44 Ahmed, D., Mao, X. L., Juluri, B. K. & Huang, T. J. A fast microfluidic mixer based on acoustically driven sidewall-trapped microbubbles. *Microfluidics and Nanofluidics* **7**, 727-731, doi:DOI 10.1007/s10404-009-0444-3 (2009).
- 45 Venancio-Marques, A., Barbaud, F. & Baigl, D. Microfluidic Mixing Triggered by an External LED Illumination. *Journal of the American Chemical Society* **135**, 3218-3223, doi:Doi 10.1021/Ja311837r (2013).
- 46 Lee, J. H., Lee, K. H., Won, J. M., Rhee, K. & Chung, S. K. Mobile oscillating bubble actuated by AC-electrowetting-on-dielectric (EWOD) for microfluidic mixing enhancement. *Sensor Actuat a-Phys* **182**, 153-162, doi:DOI 10.1016/j.sna.2012.05.022 (2012).
- 47 Lin, Y. C., Chung, Y. C. & Wu, C. Y. Mixing enhancement of the passive microfluidic mixer with J-shaped baffles in the tee channel. *Biomedical Microdevices* **9**, 215-221, doi:DOI 10.1007/s10544-006-9023-5 (2007).

- 48 Wang, S. S., Huang, X. Y. & Yang, C. Mixing enhancement for high viscous fluids in a microfluidic chamber. *Lab on a Chip* **11**, 2081-2087, doi:Doi 10.1039/C0lc00695e (2011).
- 49 Xia, H. M. *et al.* Aeroelasticity-based fluid agitation for lab-on-chips. *Lab on a Chip* **13**, 1619-1625, doi:Doi 10.1039/C3lc41346b (2013).
- 50 Johnson, T. J., Ross, D. & Locascio, L. E. Rapid microfluidic mixing. *Analytical Chemistry* **74**, 45-51, doi:Doi 10.1021/Ac010895d (2002).
- 51 Leij, F. J. & Dane, J. H. Analytical solutions of the one-dimensional advection equation and two- or three-dimensional dispersion equation. *Water Resour Res* **26**, 1475-1482, doi:10.1029/WR026i007p01475 (1990).
- 52 Hrabětová, S., Masri, D., Tao, L., Xiao, F. & Nicholson, C. Calcium diffusion enhanced after cleavage of negatively charged components of brain extracellular matrix by chondroitinase ABC. *The Journal of Physiology* **587**, 4029-4049, doi:10.1113/jphysiol.2009.170092 (2009).
- 53 Bagh, S. & Paige, M. F. Ensemble and Single-Molecule Fluorescence Spectroscopy of a Calcium-Ion Indicator Dye. *The Journal of Physical Chemistry A* **110**, 7057-7066, doi:10.1021/jp060719e (2006).
- 54 Lei, N., Li, P. F., Xue, W. & Xu, J. Simple graphene chemiresistors as pH sensors: fabrication and characterization. *Meas Sci Technol* **22**, doi:Artn 107002 Doi 10.1088/0957-0233/22/10/107002 (2011).
- 55 Li, P. F., Lei, N., Sheadel, D. A., Xu, J. & Xue, W. Integration of nanosensors into a sealed microchannel in a hybrid lab-on-a-chip device. *Sensor Actuat B-Chem* **166**, 870-

877, doi:DOI 10.1016/j.snb.2012.02.047 (2012).

- 56 Clark, A. M., Sousa, K. M., Jennings, C., MacDougald, O. A. & Kennedy, R. T. Continuous-Flow Enzyme Assay on a Microfluidic Chip for Monitoring Glycerol Secretion from Cultured Adipocytes. *Analytical Chemistry* **81**, 2350-2356, doi:Doi 10.1021/Ac8026965 (2009).
- 57 Bakker, E., Diamond, D., Lewenstam, A. & Pretsch, E. Ion sensors: current limits and new trends. *Anal Chim Acta* **393**, 11-18, doi:[http://dx.doi.org/10.1016/S0003-2670\(99\)00056-2](http://dx.doi.org/10.1016/S0003-2670(99)00056-2) (1999).
- 58 Lin, C. F., Wang, C. H., Liao, W. Y., Chou, T. C. & Lee, G. B. Hydrogen and calcium ion electrochemical detecting systems using microfluidic technology. *Micro Nano Lett* **1**, 29-33, doi:Doi 10.1049/Mnl:20065031 (2006).
- 59 Zhao, J. H., Hashmi, A., Xu, J. & Xue, W. A compact lab-on-a-chip nanosensor for glycerol detection. *Appl Phys Lett* **100**, doi:Artn 243109 Doi 10.1063/1.4729424 (2012).
- 60 Jacobs, C. B., Peairs, M. J. & Venton, B. J. Review: Carbon nanotube based electrochemical sensors for biomolecules. *Anal Chim Acta* **662**, 105-127, doi:DOI 10.1016/j.aca.2010.01.009 (2010).
- 61 Yi, C. Q., Li, C. W., Ji, S. L. & Yang, M. S. Microfluidics technology for manipulation and analysis of biological cells. *Anal Chim Acta* **560**, 1-23, doi:DOI 10.1016/j.aca.2005.12.037 (2006).
- 62 Kim, D. R., Lee, C. H. & Zheng, X. L. Probing Flow Velocity with Silicon Nanowire Sensors. *Nano Letters* **9**, 1984-1988, doi:Doi 10.1021/Nl900238a (2009).



- 63 Xue, W. & Cui, T. H. A thin-film transistor based acetylcholine sensor using self-assembled carbon nanotubes and SiO<sub>2</sub> nanoparticles. *Sensor Actuat B-Chem* **134**, 981-987, doi:DOI 10.1016/j.snb.2008.07.008 (2008).
- 64 Qu, Y. L. *et al.* Ultra-Low-Powered Aqueous Shear Stress Sensors Based on Bulk EG-CNTs Integrated in Microfluidic Systems. *Ieee T Nanotechnol* **7**, 565-572, doi:Doi 10.1109/Tnano.2008.928572 (2008).
- 65 Sia, S. K. & Whitesides, G. M. Microfluidic devices fabricated in poly(dimethylsiloxane) for biological studies. *Electrophoresis* **24**, 3563-3576, doi:DOI 10.1002/elps.200305584 (2003).
- 66 Heller, I. *et al.* Identifying the mechanism of biosensing with carbon nanotube transistors. *Nano Letters* **8**, 591-595, doi:Doi 10.1021/NI072996i (2008).
- 67 Back, J. H. & Shim, M. pH-dependent electron-transport properties of carbon nanotubes. *Journal of Physical Chemistry B* **110**, 23736-23741, doi:Doi 10.1021/Jp063260x (2006).
- 68 Rochefort, A., Avouris, P., Lesage, F. & Salahub, D. R. Electrical and mechanical properties of distorted carbon nanotubes. *Phys Rev B* **60**, 13824-13830, doi:DOI 10.1103/PhysRevB.60.13824 (1999).
- 69 Mannsfeld, S. C. B. *et al.* Highly sensitive flexible pressure sensors with microstructured rubber dielectric layers. *Nat Mater* **9**, 859-864, doi:Doi 10.1038/Nmat2834 (2010).
- 70 Sharp, A. A., Oneil, M. B., Abbott, L. F. & Marder, E. The Dynamic Clamp - Artificial Conductances in Biological Neurons. *Trends Neurosci* **16**, 389-394, doi:Doi 10.1016/0166-2236(93)90004-6 (1993).
- 71 Sharp, A. A., Oneil, M. B., Abbott, L. F. & Marder, E. Dynamic Clamp - Computer-

Generated Conductances in Real Neurons. *J Neurophysiol* **69**, 992-995 (1993).

72 Prinz, A. A., Abbott, L. F. & Marder, E. The dynamic clamp comes of age. *Trends Neurosci* **27**, 218-224, doi:DOI 10.1016/j.tins.2004.02.004 (2004).